UNIVERSITY OF OKLAHOMA

GRADUATE COLLEGE

REDUCED-ORDER 1D MODELING OF AMMONIA-FED PROTONIC CERAMIC FUEL CELLS FOR SYSTEM-LEVEL ANALYSIS

A THESIS

SUBMITTED TO THE GRADUATE FACULTY

in partial fulfilment of the requirements for the

Degree of

MASTER OF SCIENCE

By LEON RASPUDIC

Norman, Oklahoma

2026

REDUCED-ORDER 1D MODELING OF AMMONIA-FED PROTONIC CERAMIC FUEL CELLS FOR SYSTEM-LEVEL ANALYSIS

A THESIS APPROVED FOR THE

SCHOOL OF AEROSPACE AND MECHANICAL ENGINEERING

BY THE COMMITTEE CONSISTING OF:

Dr. Pejman Kazempoor, Chair

Dr. Hanping Ding

Dr. Hamidreza Shabgard

©Copyright by LEON RASPUDIC 2026
All Rights Reserved.

Contents

Abstract

Protonic ceramic fuel cells are distinguished by fuel flexibility, lower carbon emissions, scalability, and 400–650 °C operating temperatures, addressing environmental concerns while maintaining economic viability. Ammonia has been identified as a viable PCFC fuel alternative to pure hydrogen, reducing costs associated with storage and transport due to higher energy densities at more moderate temperatures and pressures. However, pure hydrogen provides more efficient electrochemical performance, raising the question of whether reduced fuel and infrastructure costs can offset the efficiency difference.

Despite the recognized potential of directly fed ammonia PCFCs, modeling efforts remain limited, with most studies relying on high-fidelity 2D/3D simulations with multi-step ammonia micro-kinetics. While accurate, these approaches are computationally intensive and impractical for system-level integration. Therefore, this work develops a one-dimensional planar PCFC model with fully coupled electrochemistry, simplified in-situ ammonia decomposition kinetics, and mass and energy conservation in Python. Ammonia decomposition is represented using a thermodynamically consistent global kinetic formulation, reducing computational cost and stiffness while preserving reaction–equilibrium coupling. The model is designed for integration into an Aspen HYSYS framework for system-level performance evaluation and technoeconomic analysis, with convergence stability improved through numerical regularization for efficient coupling with larger thermal-fluid simulation frameworks.

Results are validated through ammonia decomposition kinetics and polarization curve comparisons against literature results as well as mass and energy balance consistency checks. Polarization curves comparisons indicate $R^2 > 0.988$ and confirm predictions within 15% across all validated operating temperatures.

Furthermore, the paper presents three parametric studies based on variable ammonia inlet flow rates, average cell current densities as well as inlet temperatures, quantifying trade-offs in reactant utilization, thermal gradients, and peak power output.

Average cell current density parametric study indicates that under defined operating conditions of the PCFC, 6500 A m^{-2} current density results in the highest cell power density output of 3500 W m^{-2}. The cell experiences a sharp decrease in power output under current densities above 9000 A m^{-2}, representing less sustainable operation.

Ammonia inlet temperature parametric study indicates decomposition is strongly temperature dependent. Higher temperatures accelerate kinetics and shift the equilibrium towards products; NH_3 conversion to H_2 is more complete, sustaining electrochemical performance. NH_3 utilization ranges from 9.6% at 680K to 100% at 816K.

Nomenclature (Alphabetical)

Symbol	Description	Units
A_{active}	Active electrochemical area	m^2
A_{cat}	Catalyst area per bed volume	m^{-1}
$A_{contact}$	Contact area	m^2
A_{cs}	PEN cross-sectional area	m^2
ASR	Area Specific Resistance	$\Omega \cdot cm^{-2}$
C	Defined inlet species ratio	-
c_p	Specific heat capacity	$J \cdot kg^{-1} \cdot K^{-1}$
D	Binary gas coefficient	$m^2 \cdot s^{-1}$
d_h	Hydraulic diameter	m
E_{Nernst}	Nernst (equilibrium) potential	V
F	Faraday constant	$C \cdot mol^{-1}$
h	Convective heat transfer coefficient	$W \cdot m^{-2} \cdot K^{-1}$
I_{cell}	Electrical current	A
j_0	Exchange current density	$A \cdot m^{-2}$
$j_{cell,avg}$	Average cell current density	$A \cdot m^{-2}$
j_i	Local current density at axial segment i	$A \cdot m^{-2}$
K_{eq}	Equilibrium constant	-
k_{NH3}	Kinetic rate constant	$mol \cdot Pa \cdot m^{-2} \cdot s^{-1}$
k_{th}	Thermal conductivity	$W \cdot m^{-1} \cdot K^{-1}$
L	Channel length	m
$\ln(\hat{k}_{NH3})$	Hydrogen inhibition coefficient	$\sqrt{Pa}$
N	Number of discretization segments	-
Nu	Nusselt number	-
$\dot{n}$	Molar flow rate	$mol \cdot s^{-1}$

P	Species partial pressure at channel	Pa
P_{cell}	Total pressure	Pa
p_{dens}	Cell power density	$W \cdot m^{-2}$
Pr	Prandtl number	-
P_{TPB}	Species partial pressure at triple phase boundary	Pa
$\dot{q}_{cond}$	Conductive heat transfer	W
$\dot{q}_{conv}$	Convective heat transfer	W
$\dot{q}_{rxn}$	Heat generated/consumed by reactions	W
Re	Reynolds number	-
R_g	Universal gas constant	$J \cdot mol^{-1} \cdot K^{-1}$
r_{NH3}	Intrinsic ammonia decomposition reaction rate	$mol \cdot m^{-3} \cdot s^{-1}$
$R_{PEN \rightarrow IC}$	Thermal resistance between PEN and IC	$K \cdot W^{-1}$
RR	Reaction rate	$mol \cdot s^{-1}$
R_{total}	Total thermal resistance between PEN and IC	$K \cdot W^{-1}$
T	Temperature	K
T_{air}	Air channel temperature	K
T_{fuel}	Fuel channel temperature	K
T_{IC}	Interconnect temperature	K
T_{PEN}	PEN temperature	K
u	Fluid velocity	$m \cdot s^{-1}$
V_{cell}	Operating cell voltage	V
y	Species molar fraction	-
Z_k	Charge number	-

ΔG_{rxn}	Reaction Gibbs free energy	$J \cdot mol^{-1}$
ΔH_{rxn}	Reaction enthalpy change	$J \cdot mol^{-1}$
ΔS	Entropy change	$J \cdot mol^{-1} \cdot K^{-1}$
Δz	Axial segment length	m
ε_p	Smooth max offset	-
η_{act}	Activation overpotential	V
η_{conc}	Concentration overpotential	V
η_{ohmic}	Ohmic overpotential	V
μ	Dynamic viscosity	$Pa \cdot s$
ν	Stoichiometric coefficient	-
ρ	Density	$kg \cdot m^{-3}$
τ	Thickness	m
$\dot{\omega}$	Molar production or consumption of species	$mol \cdot s^{-1}$

Subscripts

an	Anode
c	Fuel or air channel
ca	Cathode
i	Axial discretization index
k	Species
ORR	Oxygen Reduction Reaction
PEN	Positrode, Electrolyte, Negatrode
s	Smooth max function regularization
TPB	Triple Phase Boundary

1) Introduction

Following section outlines the role of protonic ceramic fuel cells in the green energy transition, with an emphasis on the application of ammonia as a hydrogen carrier. It further frames the application of modeling and its importance in implementation of the technology, especially regarding system level analysis development. Furthermore, relevant previous research is outlined and a gap in computationally efficient mechanistic modeling is identified.

1.1) Background

Greenhouse gas emissions associated with utilization of fossil fuels for power generation are identified as the leading factor in global warming. Growing demand, accelerated by industrialization and population growth, has intensified the reliance on fossil fuels, further exacerbating climate change. Average yearly surface temperatures have been increasing by approximate 1.6 °C since the late 19th century, with a sustained yearly growth pattern occurring from the late 1970s [1].

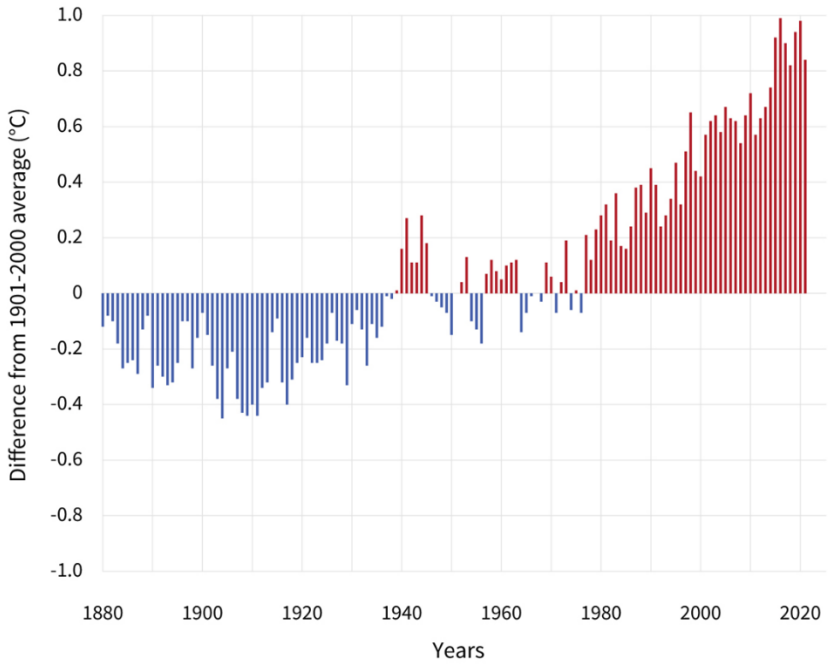

Figure 1 Global Average Surface Temperature Difference (1880 - 2020), adapted from [2]

Globally, energy use (electricity, heat industry and transport) contributed approximately three quarters of the global greenhouse gas emissions, associated with CO_2 emissions increasing by 0.8% in 2024 [3]. Transition from fossil fuels requires diversification of energy infrastructure and focus on a variety of carbon neutral sources of energy. Fuel cells have the potential to occupy a significant position in the green energy transition due to a wide scope of identified applications. While utilization for sole power generation is still limited, fuel cells have emerged as a prospective technology in electrical grid stabilization, energy storage, cogeneration in complex energy systems, power backup etc. [4]. They are distinguished by fuel flexibility, scalability and negligible carbon emissions depending on hydrogen source, addressing environmental concerns while maintaining economic viability[5].

However, several issues represent obstacles in large scale implementation of fuel cells, primarily concerning manufacturing and implementation costs, efficiency, durability and

chemical stability [6], [7]. High manufacturing costs are offset by rare earth metals used for catalysts, electrolyte materials, complex manufacturing techniques etc. Secondly, several fuel cell types such as SOFCs typically operate at temperatures higher than 900K to facilitate reaction kinetics [8]. These high operating temperatures increase thermal stresses, accelerate material degradation, and introduce system-level challenges related to thermal management and startup requirements. Furthermore, the relatively slow thermal response of SOFCs limits their suitability for rapid load-following and short-timescale grid stabilization applications.

Protonic ceramic fuel cells have raised significant attention due to addressing several issues outlined previously. PCFCs operate at lower temperatures (400°C-600°C) compared to oxygen ion conducting SOFCs (700°C-1000°C) [9], [10], [11]. The lower operating temperature mitigates the thermal stress the fuel cell is exposed to, lowering degradation rates and improving material durability [11]. Moreover, lower temperatures additionally reduce the startup times and improve dynamic responses to grid supply and demand fluctuations.

However, the overarching challenge in the large-scale implementation of fuel cells into the existing energy framework is the high capital and operational expenses of the hydrogen infrastructure, exacerbated by hydrogen's low energy density [12]. Due to the low energy density per volume, hydrogen needs to be either compressed at pressures up to 800 bar or liquified at temperatures below 20.28 K [13]. The energy requirements needed to maintain the system under operational parameters offsets the operational expenses.

Hydrogen infrastructure would require extensive storage systems to buffer variability in production and demand, with system-level analyses suggesting that storage capacities corresponding to a significant fraction of production [14].

In addition, a large transportation network would be required consisting of specialized pipelines, high-pressure compressors, liquefaction and cooling systems as well as safety control equipment. Such infrastructure demands high capital investment and long development timelines, representing a major barrier to large scale hydrogen deployment [15].

Using alternative fuels has been identified as a solution to mitigate the high capital and operational costs of a pure hydrogen infrastructure. Various studies have explored fuel cell operation with different fuels such as natural gas, methanol, ethanol, propane, and ammonia [16], [17], [18].

One promising alternative to the use of pure hydrogen in fuel cell energy technologies is ammonia. With its boiling point of -33 °C at 1 bar, ammonia requires a significantly lower energy input for storage and transportation compared to hydrogen [19]. In addition, ammonia production and transport are supported by already developed logistics, having approximately 8000 km of dedicated pipelines as of 2023, marine carriers and railways, decreasing costs associated with future integration of energy infrastructure.

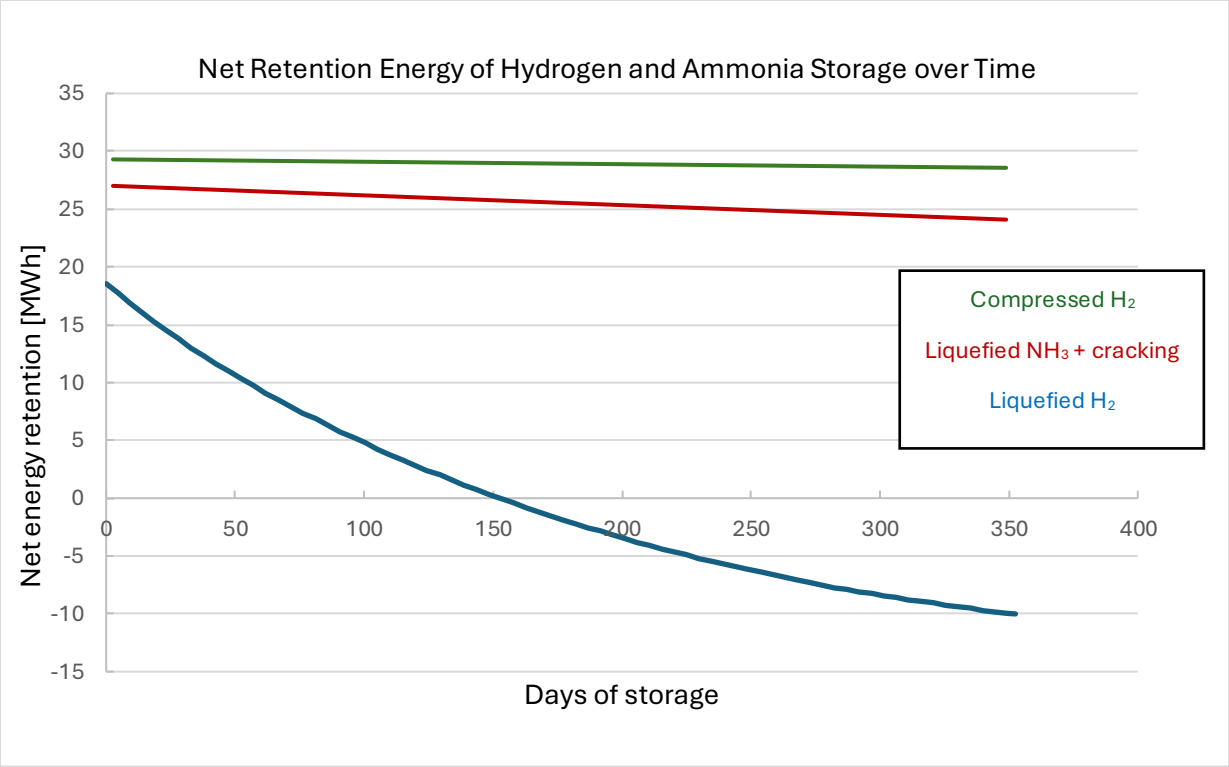

Figure 2 Net Energy Retention of Hydrogen and Ammonia Storage Pathways as a Function of Storage Duration, adapted from [20]

As each metric ton of hydrogen can supply a maximum of 33.6 MWh of energy, Figure 2 represents the net share of energy after subtracting the daily energy costs associated with storage including compression, liquefication and cracking as well as boil off [20]. Although compressed hydrogen exhibits the highest net energy retention due to the absence of liquefaction and conversion penalties, this does not account for its low volumetric energy density and associated storage and transport challenges. Consequently, alternative carriers such as ammonia may offer system-level advantages despite slightly lower energy efficiency.

Application in PCFCs is possible as the operating temperature is in the range of the decomposition temperature of ammonia. Introducing catalysts such as nickel to the anode

further promotes the reaction. Additionally, PCFCs have demonstrated stable operation under ammonia fuel in contrast to SOFCs which have been associated with voltage instability and performance degradation due to nickel nitridation and phase instability [21].

Several studies indicate that PCFCs operating on ammonia underperform those operating on pure hydrogen in terms of power density, overpotentials, Faradaic efficiency etc. However, these comparisons typically overlook the lower energy requirements associated with ammonia storage and transportation, which requires further system level analysis.

1.2) Literature Review

Previous research on ammonia-fed protonic ceramic fuel cells has placed more focus on developing high fidelity 2-D models capturing complex PCFC mechanisms in detail, with system level studies tending to develop simplified 0-D approximations.

Zhu et al. [22] developed a multiscale PCFC button cell model consisting of transient 3D thermal, 1D channel flow, and 1D membrane–electrode assembly (MEA) electrochemical sub-models. The fuel cell electrochemistry is expressed through the electrolyte lattice defect conservation equations. Defect transport is described through the Nernst-Planck model capturing the impact of defect concentrations and electrolyte electrical field on charge transportation. The current density is obtained directly from the charge-weighted sum of defect fluxes, rather than through an assumed conductivity. This formulation enables simulating the mixed ionic-electronic charge transport through PCFC electrolytes, giving a more accurate description of electrical conductivity and losses. Additionally,

multispecies diffusion transport through the porous electrodes is described using the Dusty gas model, simultaneously capturing molecular diffusion, Knudsen diffusion, and viscous (pressure-driven) flow. Zhu defines ammonia decomposition as a multi-step process described through a system of site coverage ODEs. This simulates the site coverage of each intermediate state, giving insight into which step limits the overall decomposition reaction. Overall, this is a foundational model which provides detailed insight into coupled behavior of PCFC states. However, the level of detail greatly increases the computational intensity making it less adequate for system level analysis.

Li et. al. [23] developed a micro-tubular 2-D model focusing on studying ammonia-fed PCFC performance under differing operating conditions. The model simplifies the electrochemical model by assuming defect equilibrium; instead of solving evolving defect concentrations, they are determined by local cell operating conditions such as pressure and temperature. Thus, defect concentrations are obtained by solving a system of algebraic relations defined by defect reaction equilibrium constants, where the equilibrium constants are evaluated from thermodynamic enthalpy and entropy data, and the solution is constrained by electroneutrality, oxygen-site conservation, and polaron conservation conditions. Similar to Zhu et. al. the paper models charge transport using Nernst-Planck formulation, multi-species electrode transport is defined through the Dusty gas model and ammonia decomposition kinetics are described using a multi-step decomposition process. This model simplifies the approach taken by Zhu, assuming defect concentrations are governed by reaction equilibria, reducing complexity associated with transient defect transport. However, it retains the complex Nernst-Planck formulation, Dusty gas for electrode species

diffusion as well as multistep ammonia decomposition reaction description. Thus, the model remains computationally intensive and limited suitability for system level integration.

Zhu et. al. [24] developed a reduced order power-heat-freshwater trigeneration system utilizing ammonia-fed protonic ceramic fuel cell, micro gas turbine, and air gap membrane distillation. The fuel cell model makes simplifying assumptions to reduce the computational intensity and enable integration into a system level framework. The model calculates current density based on an algebraic voltage balance, where the operating voltage is expressed as the difference between the Nernst potential and the sum of concentration, activation and ohmic overpotentials. This approach avoids explicitly modeling charge transport kinetics using lattice defect conservation and flux equations (e.g., Nernst–Planck formulation), instead relying on semi-empirical relationships to represent electrochemical behavior, thereby significantly reducing model stiffness and computational cost while maintaining suitability for system-level performance and optimization studies. The cell is modeled as a 0-D stack, with no axial temperature, species and current density discretization, meaning that the model only captures average cell behavior rather than local physicochemical phenomena. This can impact performance prediction, as the model cannot capture the coupled spatial evolution of species concentrations and temperature arising from local generation and consumption processes, nor can it identify regions of limiting reactant availability within the cell. Additionally, ammonia decomposition is expressed through a first order Arrhenius relationship, assuming no hydrogen inhibition occurs at high fuel cell operating temperature. This can cause performance overprediction as it cannot capture the effects of incomplete decomposition and equilibrium limited

regions. While the PCFC model is simplified and less computationally intensive, it does not account for spatially evolving fuel cell behavior, which can limit performance insight.

Overall, most publications on ammonia-fed PCFCs focus on developing high fidelity, mechanistic models. Such modeling efforts require constructing complex, tightly coupled, nonlinear equation systems which can introduce solution stiffness as well as high computational load. Consequently, these models are less suitable for large-scale parametric studies, control-oriented simulations, or design optimization, where reduced-order coupled formulations are typically required to ensure numerical robustness and tractability.

On the other hand, models developed for system level analysis have been comparatively more limited in number and often do not capture spatially resolved interactions between transport, electrochemical reactions, and ammonia decomposition within the cell. Furthermore, these models are frequently developed for a specific application or operating conditions which can limit their generalizability and applicability in different system configurations.

This motivates the development of simplified, spatially discretized models capturing the evolution of key PCFC states such as temperature, pressure and species' molar flows, governed by the interacting electrochemical reactions, ammonia decomposition kinetics and transport phenomena. Overall, this approach provides a physically consistent, spatially resolved PCFC modeling framework that enables assessment of the impact of spatial

variations in key state variables on both cell- and system-level performance, while maintaining a balance between physical fidelity and computational tractability.

1.3) PCFC Overview

Protonic Ceramic Fuel Cells (PCFCs) are a subclass of solid-state electrochemical energy conversion devices converting the chemical energy of a fuel directly into electricity through electrochemical reactions [17].

A single protonic ceramic fuel cell (PCFC) is a multilayer electrochemical device composed of flow channels, interconnect layers, and a membrane–electrode assembly.

Two flow channels are on each side of the cell, supplying reactants to the electrodes and removing unreacted species and products.

Interconnects provide electrical connection between adjacent cells and serve as current collectors. Two interconnects are present: one separating the fuel channels and the other separating the air channels.

The membrane–electrode assembly which will be referred to as PEN consists of a porous cermet anode and porous ceramic cathode separated by a dense proton-conducting perovskite electrolyte. The contact area between the electrodes and the electrolyte is known as the triple phase boundary (referred to as TPB in the paper).

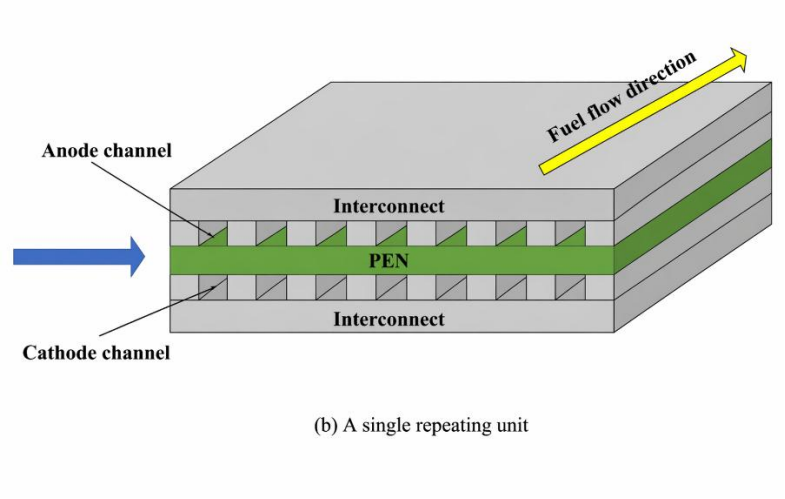

Figure 3 Simplified PCFC diagram with annotated elements, Adapted from [25]

PCFC electrolytes enable transport of protons while blocking conduction electrons, thereby separating the charges and directing the electrons through an external circuit.

In galvanizing mode, the electrochemical oxidation of hydrogen at the anode involves dissociative adsorption of H_2, charge transfer to the anode catalyst, and proton incorporation into the electrolyte at the **triple-phase boundary**.

$$H_2 \rightarrow 2H^+ + 2e^- \quad (1)$$

At the cathode, oxygen molecules undergo surface dissociation, are reduced by electrons supplied by the external circuit and react with hydrogen protons to form water.

$$\frac{1}{2}O_2 + 2H^+ + 2e^- \rightarrow H_2O \quad (2)$$

Under steady-state operation, the rates of the anodic and cathodic reactions must be equal to ensure charge conservation and maintain a consistent current density throughout the cell.

Note that actual electrolytes are mixed ionic-electronic conductors meaning that electronic holes can be transported in addition to positive charge, introducing current leakage. In this paper, it is assumed that the electrolyte is ideal, therefore only positive charge is accounted for in the electrochemical model.

PCFCs can operate under a variety of fuels ranging from pure hydrogen, ammonia, ethanol, and hydrocarbons such as methane, ethane etc. Hydrocarbon or ammonia-based fuels must be cracked or reformed into hydrogen before electrochemical oxidation. In a PCFC, this is achieved either through direct integration at the anode or via an upstream pre-reformer, depending on the fuel's thermal requirements. In direct fuel cracking, the fuel is absorbed onto the active sites of the anode where it undergoes catalytic dissociation. Catalysts such as nickel decrease the activation energy necessary to break the molecular bonds and “free” the hydrogen to further participate in electrochemical reactions.

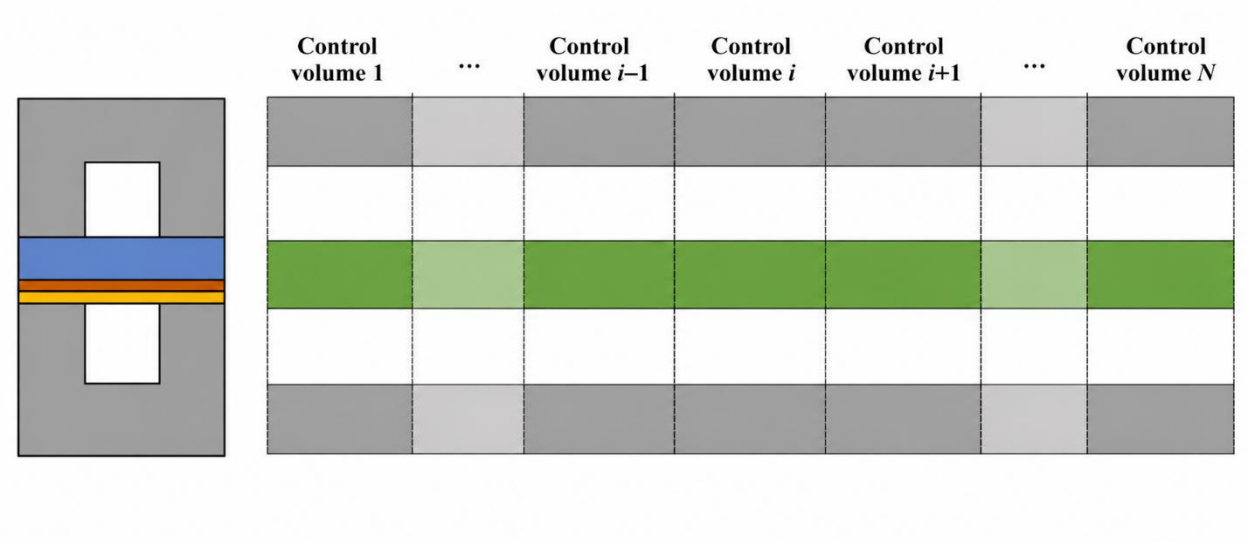

Figure 4 PCFC channel front and side cross sections with annotated reaction processes, adapted from [25]

Ammonia-fed PCFCs are governed by strongly coupled electrochemical reactions, species transport mechanisms, ammonia decomposition kinetics, and thermal effects. As a result, the system behavior is described by a set of nonlinear, coupled equations that must be solved iteratively to obtain a consistent solution. In the present model, the primary state variables include temperature, species molar flow rates, and current density since they can fully define the behavior of the outlined fuel cell processes. Note that state variables are bidirectionally coupled with respective reaction mechanisms. For example, state variables such as temperature and species molar flow influence the electrochemical and chemical reaction rates. These reactions will further impact the molar flows and temperature as species participate in reactions and heat is generated or consumed. This causes evolving behavior throughout the cell which impacts the overall performance. Models are discretized to resolve spatial variation in cell behavior, enabling simulation of evolving state variables along the cell.

2) Modeling

Following chapter provides a detailed overview of assumptions, electrochemical, energy balance, mass balance, ammonia decomposition and thermochemical property formulation. These components are integrated within a reduced-order, one-dimensional framework to capture the coupled transport, reaction, and electrochemical processes governing cell performance. Lastly, solver architecture is introduced, describing how the resulting nonlinear system is resolved and which numerical methods are implemented to improve model convergence.

2.1) Modeling Assumptions and Geometrical Representation

The PCFC solver consists of coupled electrochemical, ammonia decomposition kinetics, mass and energy conservation sub models. The model is based on 10 state variables including cell voltage, current density, molar flow rates of H_2, O_2, H_2O, NH_3 as well as fuel, air, interconnect and lumped PEN temperatures. The cell voltage and local current density are obtained by solving the nonlinear residual equations defined in the electrochemical sub model. Hydrogen, oxygen, and water molar flow rates are determined from discretized mass conservation equations coupled with electrochemical reaction rates. Ammonia molar flow is determined from a thermo-catalytic reaction sub model. The fuel-side temperature, air-side temperature, as well as interconnect and lumped PEN temperature are computed from the energy balance residuals defined in the energy sub model.

This is a nonlinear coupled multiphysics systems problem consisting of 9*N+4 unknowns. The nonlinear algebraic system is solved using a Newton-type method implemented through SciPy's fsolve, which employs a modified Powell hybrid algorithm [26].

Note that numerical solvers based on the Newton method may fail to find a converging solution when encountering discontinuities in governing equations. Techniques such as tanh smoothing [27] and continuous max functions are utilized to facilitate transitions between piecewise functions, which is further described in section 2.8). In addition, the solver is sensitive to strong nonlinearity between variables and bad initial guesses. To improve convergence, the solution is initialized using physically reasonable estimates, and variable scaling is applied where necessary to ensure numerical stability.

The PCFC is modeled using a planar geometry, where cell components are arranged as flat layered structures. The model distinguishes between interconnect, fuel and air channels and lumps positive electrode, electrolyte, negative electrode structure (PEN) as a single element [25], [28]. This assumption simplifies the representation of interactions between the gas channels and the solid structures by avoiding the need to resolve separate temperature and state profiles within each PEN component. In addition, there is no variation along the thickness of the cell components.

Flow in the fuel and air channels is assumed to be fully developed and laminar, consistent with the low Reynolds numbers characteristic of planar fuel cell channel geometries at the modeled operating conditions [29]. In addition, cross-sectional velocity gradients are not

resolved, instead a uniform average velocity is used for bulk transport calculations along the axial direction.

Overall, this simplification avoids solving 2D/3D Navier-Stokes and boundary layer equations for the bulk channels, reducing model complexity and computational load [30].

For the PEN, assuming variables are uniform across its thickness avoids resolving localized electrochemical and chemical reaction rates, simplifying species molar flow and thermal modeling.

Additionally, the variables are assumed to vary only along the axial direction, with lateral variations considered negligible. This implies that there are no hotspot localizations, secondary flows, channel/rib interactions etc.

The system is approximated as adiabatic, neglecting net heat exchange with the surroundings [30]. This assumption is representative of interior cells in large fuel cell stacks, where temperature gradients between neighboring cells are small and external heat losses are negligible compared to internal heat generation and conduction.

The plates are considered as equipotential, assuming that both electrodes are good conductors, resulting in negligible in-plane voltage gradients and eliminating the need to explicitly resolve charge transport within the electrode structures [29], [31]. This enables representing the cell with a single global electrical potential while allowing current density to vary spatially along the flow direction [29].

The model reduces the spatial dimensionality of the fuel cell from a fully three-dimensional representation to a quasi-one-dimensional formulation discretized along the flow direction. In this approach, complex geometric features such as multiple parallel flow channels distributed across the PEN surface are represented by an equivalent, area-averaged structure. Specifically, the simplified geometry is constructed such that the total flow cross-sectional area and characteristic dimensions correspond to the sum of the individual channel contributions.

This representation enables the treatment of the fuel cell as a single effective flow path, while assuming negligible spatial gradients in the lateral directions. As a result, variations in species concentrations, temperature, and electrochemical activity are resolved only along the axial direction, whereas transverse non-uniformities are not explicitly captured. Importantly, through-plane transport processes, including electrochemical reactions and proton conduction across the PEN structure, are retained through geometry-dependent source terms rather than spatially resolved thickness discretization.

Additionally, the model represents the fuel and air side interconnects as a single lumped element with a uniform axial temperature distribution, rather than resolving each plate individually. Lumping them into one element assumes that the temperature difference between the two plates is small relative to the overall thermal gradients in the cell. This simplification avoids introducing separate energy balance equations for each interconnect plate, reducing model complexity while retaining the primary thermal role of the interconnect as a conductor of ohmic heat and a mediator of heat exchange between the solid cell structure and the gas streams.

To preserve the physical consistency of the model, it is therefore essential that geometric parameters such as active area, gas channel cross-sectional area, interconnect dimensions, PEN layer thicknesses, and contact areas are defined based on realistic cell designs. These parameters directly govern the scaling of mass, charge, and energy transport processes, ensuring that the reduced-order model accurately reflects the underlying system behavior despite the dimensionality reduction.

The fuel cell geometric design specifications are further described in section 2.7.1)

2.2) PCFC Electrochemical Performance

The electrochemical model describes the conversion of chemical energy into electrical energy through oxidation and reduction reactions occurring at the electrodes. This enables evaluating the overall cell performance through determining the maximum theoretical potential, accounting for electrochemical losses as well as predicting the resulting operating voltage and power output. Hence, this facilitates choosing operating parameters which result in highest operating efficiency. As stated in the modeling assumptions section 2.1), there is no axial variation in electrical potential across the electrodes, which is also known as the equipotential assumption.

The model computes axially varying current densities $j_{cell,i}$ and a corresponding uniform cell potential V_{cell}. The average current density value is treated as an input which the model uses to find an array of current density values at each discretized point. The individual discretized points are defined through a set of electrochemical relationships which ultimately yield a constant electrical potential value across the entire cell.

In total, there is N j_{cell} outputs corresponding to each discretized point in the model as well as a single V_{cell} output for the entire cell.

This formulation differs from approaches that assume a uniform current density across the cell, which can neglect the impact of spatially varying operating conditions on local reaction rates and lead to less detailed performance predictions. Conversely, more detailed formulations that simultaneously solve both spatially varying current density and electrical potential require resolving in-plane charge transport, introducing additional governing equations and increasing computational complexity [22]. Under the defined solver architecture, careful selection of operating conditions is required to ensure physically meaningful solutions. Since the model enforces a global cell voltage while solving for the spatial distribution of current density, it may converge to mathematically consistent solutions even under conditions that are not physically realizable.

In contrast, formulations that simultaneously solve for both voltage and current density inherently impose stricter physical constraints, which can prevent convergence under infeasible operating conditions.

General electrochemistry architecture has been adopted from the work by Norman et. al. [18], with formulation being adapted to reflect ammonia fed PCFC material properties and operating principles. Most published models describe electrochemistry based on defect transport calculated from the Nernst-Planck formulation. Alternatively, models use an empirical expression based on experimental data which lumps loss mechanisms. Approach developed by Norman expresses electrochemistry through a simplified mechanistic model,

giving insight into interdependence with energy and mass sub models. The model design treats impact of hydrogen presence at the fuel channels and reacting areas separately, decoupling bulk thermodynamic influences on equilibrium potential from local kinetic and mass transport effects. However, the formulation still does not completely capture PCFC processes such as MIEC mechanistically, as outlined in sections 1.3). Instead, effects can be indirectly accounted for through empirical correlations based on experiments.

$$E_{Nernst,i} - \eta_{act,i} - \eta_{conc,i} - \eta_{ohm,i} - V_{cell} = 0 \tag{3}$$

E_{Nernst} is the thermodynamic equilibrium potential, η_{act} is the activation overpotential, η_{conc} is the concentration overpotential, η_{ohm} is the ohmic overpotential, and V_{cell} is the operating cell voltage.

To solve the system, we need to define the average current density residual function:

$$j_{\mathrm{cell,avg}} - \frac{1}{N}\sum_{i=1}^{N} j_{\mathrm{cell},i} = 0 \tag{4}$$

where $j_{\mathrm{cell,avg}}$ is the prescribed average current density across the cell, $j_{\mathrm{cell},i}$ is the local current density at discretized point i, N is the total number of discretization points, and $\frac{1}{N}\sum_{i=1}^{N} j_{\mathrm{cell},i}$ is the arithmetic mean of the local current density distribution. Local or segment current density needs to be distinguished from total segment current which is expressed as:

$$I_{\mathrm{cell,i}} = j_{\mathrm{cell,i}} \cdot A_{active} \tag{5}$$

Cell current density is typically used to describe the performance of the PCFC, as it represents cell operation independently of model size parameters, which facilitates comparisons with other developed models.

2.2.1) Nernst Potential

The maximum operating voltage of the fuel cell is calculated through the Nernst equation. This paper uses the modified gas-based form accounting the impact of operating pressures and species chemical potentials of the PCFC.

$$E_{\text{Nernst}}(i) = -\frac{\Delta G_{\text{ORR}}(i)}{2F} + \frac{R\,T_{\text{PEN}}(i)}{2F}\ln\left[\frac{\left(P_{H_2,\text{s}}(i)/P_{\text{cell}}\right)\sqrt{P_{O_2,\text{s}}(i)/P_{\text{cell}}}}{P_{H_2O,\text{s}}(i)/P_{\text{cell}}}\right] \quad (6)$$

where ΔG_{orr} is the Gibbs free energy for the water formation reaction , $P_{H_2,s}$, $P_{O_2,s}$, $P_{H_2O,s}$ represent the regularized partial pressures of hydrogen on the fuel side as well as the oxygen and water on the air side respectively, described in section 2.4). The subscript s indicates that the values are regularized to a positive range through a continuous maximum approximate function (76), P_{cell} represents the cell pressure used to normalize the logarithmic term and is assigned as an input. For the water formation reaction, $n = 2$ since there are 2 protons required for the reaction. Note that Gibbs free energy of the ORR is a variable dependent on the system state and is computed for each discretized point, as described in section 2.6).

The Nernst equation captures the thermodynamic impact of fuel channel hydrogen levels on cell electrochemical performance. In the present model, the hydrogen partial pressure used in the Nernst expression is evaluated from the bulk fuel channel composition,

representing the average reactant availability. Reducing hydrogen levels lowers the thermodynamic driving force for the electrochemical reaction, resulting in a lower voltage across the cell length.

In equation (3) electrochemistry is described through three loss mechanisms: activation, concentration and ohmic losses, governing the operating voltage of the cell [18], [30]. The contribution of each loss mechanism may change throughout the cell as the state variables evolve. The individual loss mechanisms are described in the following sections.

2.2.2) Activation overpotential

Activation overpotential represents the losses incurred to overcome the oxidation and reduction reaction energy barriers [32]. In electrochemical reactions, electrical work related to applying an overpotential to an electrode lowers the reaction activation energy. In PCFCs, lowering the activation energy increases the rate at which hydrogen is reduced, leading to an increase in current density [32]. However, this reduces the operating voltage of the fuel cell, meaning that the electrons travelling through the external circuit will carry less energy. The relationship between the cell current density and activation overpotential is described by the Butler-Volmer equation [22], [23].

$$j_{cell} = j_0 \left[\exp\left(\frac{\alpha_a n F \eta}{RT}\right) - \exp\left(-\frac{\alpha_c n F \eta}{RT}\right) \right] \tag{7}$$

where j_{cell} is the net current density, j_0 is the exchange current density, $\alpha_a$is the anodic charge-transfer coefficient, $\alpha_c$is the cathodic charge-transfer coefficient, $n$is the number of electrons transferred in the reaction, $F$is Faraday's constant, $\eta$is the activation

overpotential, $R$is the universal gas constant, and T is the electrode temperature. Under the model assumption, $T = T_{PEN}$ since electrodes are considered lumped.

The exchange current density j_0 represents the intrinsic charge-transfer kinetics at the electrodes [32]. It is the reaction rate at equilibrium when no overpotential is applied to the fuel cell. It is calculated using [23], [29]:

$$j_{0,\text{electrode}} = \frac{RT}{nF} k_{\text{electrode}} \exp\left(-\frac{E_{\text{electrode}}}{RT}\right) \tag{8}$$

where $j_{0,\text{electrode}}$ is the electrode exchange current density, R is the universal gas constant, $T$is the absolute temperature, n is the number of electrons transferred in the electrochemical reaction $k_{\text{electrode}}$ is a kinetic prefactor and $E_{\text{electrode}}$ is the effective activation energy barrier for the electrode reaction.

Note that the reaction kinetics are different for the anode and cathode due to different reactions kinetics, materials, etc. Hence, $j_{0,\text{electrode}}$ is evaluated for each electrode separately, the activation energy barrier parameters being based on the work by Zhu et. al. [33] while the preexponential factors are based on works by Sahli et al. [34] and Zhang et. al. [32]

$$j_{0,\text{ca}} = 8.817 \times 10^9 \exp\left(-\frac{43360}{R\,T_{PEN,i}}\right) \tag{9}$$

$$j_{0,\text{an}} = 9.577 \times 10^8 \exp\left(-\frac{83000}{R\,T_{PEN,i}}\right) \tag{10}$$

Note that in PCFCs, the cathode oxygen reduction reaction is more complex than the anode hydrogen oxidation due to stronger covalent O=O bonds, multi-electron transfer and the

need for oxygen adsorption, dissociation and incorporation [35]. This is reflected in a lower exchange current density value, typically leading to a higher activation potential loss at the cathode, representing the rate-limiting reaction mechanism in PCFCs.

The model utilizes a simplified hyperbolic sine approximation for the Butler Volmer equation [29]. Implementing the Butler–Volmer equation in its original implicit form would require introducing an additional residual equation for the activation overpotential, as the equation is not easily analytically invertible in closed form with respect to overpotential. However, introducing the hyperbolic sine functions implies that the symmetry factors α_a, α_c equal 0.5 each [36], reducing insight into individual electrode overpotential contributions stemming from kinetic asymmetry, albeit reducing the solver stiffness.

$$\eta_{\text{act},i} = \frac{2RT_{PEN,i}}{F}\sinh^{-1}\left(\frac{j_{cell,i}}{2j_{0,an,i}}\right) + \frac{2RT_{PEN,i}}{F}\sinh^{-1}\left(\frac{j_{cell,i}}{2j_{0,ca,i}}\right) \tag{11}$$

2.2.3) Concentration Overpotential

Concentration losses arise from resistance to mass transport of reacting species within the electrodes [36]. During operation, fuel and oxidant species must diffuse through the porous electrode structure to reach active reaction sites, where they react in the presence of catalysts and other participating species [36]. These losses are exacerbated when reactant consumption outpaces transport, leading to local concentration gradients [36]. Non-uniform electrode microstructure, degradation or wear, and spatially varying reaction kinetics can further intensify concentration losses by causing uneven reactant distribution, which limits access to active sites and reduces the effective reaction rate. Increasing

current density increases the concentration losses as the reactant consumption rate is higher than the diffusion rate through the electrode [36]. The calculation approach is adapted from Aguiar et. al. with modifications for a PCFC.

$$\eta_{conc} = \frac{RT_{PEN}}{2F}\left[\ln\left(\frac{P_{H_2,s}}{P_{H_2,s}^{TPB}}\right) + \ln\left(\frac{P_{H_2O}^{TPB}\cdot\sqrt{P_{O_2,s}}}{P_{H_2O}\sqrt{P_{O_2,s}^{TPB}}}\right)\right] \tag{12}$$

Where η_{conc} is the concentration overpotential, T_{PEN} is the local PEN temperature, $P_{H_2,s}$, $P_{H_2O,s}$, and $P_{O_2,s}$ are the regularized bulk partial pressures of hydrogen, water, and oxygen, respectively, $P_{H_2,s}^{\mathrm{TPB}}$, $P_{H_2O,s}^{\mathrm{TPB}}$, and $P_{O_2,s}^{\mathrm{TPB}}$are the corresponding partial pressures at the triple-phase boundary (TPB).

Concentration losses are governed by species partial pressures at the electrode-electrolyte interfaces. While Dusty gas model or Maxwell equations may represent the partial pressure evolution through a porous multispecies electrode environment with higher fidelity [22], [23], the high complexity and computational costs render these equations difficult to implement in a Python environment. Aguiar derives the TPB species partial pressure expressions through Fick's law, describing species diffusion as proportional to local concentration gradients. Expressing Fick's law through Faraday equations to find the species partial pressures at the TPB yields:

$$P_{O_2}^{TPB} = P_{O_2} - \frac{RT\tau_{ca}}{4FD_{ca}}j_{cell} \tag{13}$$

$$P_{H_2O}^{TPB} = P_{H_2O} + \frac{RT\tau_{ca}}{2FD_{ca}}j_{cell} \tag{14}$$

$$P_{H_2}^{TPB} = P_{cell} - \left(P_{cell} - P_{H_2}\right)\exp\left(\frac{RT\tau_{an}}{2FD_{an}P_{cell}} * j_{cell}\right) \tag{15}$$

Where τ_{ca} and τ_{an} are the cathode and anode thicknesses, while D_{ca}, D_{an} are the binary gas coefficients. The implementation of hyperbolic tangent and continuous max smoothing is further described in 2.8)

Note that the framework developed by Aguiar et. al. does not fully represent the operating conditions in this model. The Aguiar et. al. approach is adapted for two or less electrochemically reacting species per channel, while current model has additional non electrochemically participating species such as nitrogen and ammonia. Unlike Stefan-Maxwell diffusion or DGM which can model multispecies diffusion, Fick's law can be only used as an approximation, since it may not model multispecies diffusion as accurately [37]. The current formulation may misrepresent the concentration overpotential, as it assumes that the only driving force of diffusion is species concentration gradients. In reality, diffusion in multicomponent systems is coupled, accounting for concentration gradients and interactions between species [37].

2.2.4) Ohmic overpotential

The ohmic overpotential arises from resistance to charge transport within the PCFC components and is primarily attributed to the electrolyte and interconnect layers. The resistance is dependent on conductor temperature and typically calculated using a lumped empirical expression also known as area specific resistance (ASR). Albrecht et. al. [28] provided an overall cell ASR function based on electrochemical impedance spectroscopy measurements for multiple stream composition. The paper utilizes ASR data from the 97% H2 3% H2O condition as it is the closest to the operating conditions of the cell.

$$ASR_i = 0.0039 \cdot e^{3.9551 \cdot \frac{1000}{T_{PEN,i}}} \quad (16)$$

2.3) PCFC Energy Balance

The energy balance sub model consists of 4*N residual equations describing the steady state heat transfer mechanisms between the PEN, interconnect, fuel and air channels. The balances enable calculation of evolving temperatures at each element. The relationships are formulated using a consistent sign convention to ensure energy conservation at each discretized control volume.

2.3.1) PEN structure energy balance

Several heat transfer mechanisms impact the temperature of the PEN structure; axial conduction inside the PEN, interfacial conduction between the PEN and the interconnect, convective heat transfer with the bulk channels, heat generation by the ORR and heat consumption by ammonia decomposition. Note that radiation heat transfer between the PEN and the interconnect is neglected to reduce model nonlinearity stemming from the T^4 term as it has a negligible effect on heat transfer and cell performance [29], [30], [38]. The resulting energy balance is formulated as a nonlinear steady-state one-dimensional heat transfer equation, incorporating axial conduction and distributed source terms representing heat generation and consumption within the cell.

$$k_{th,PEN} A_{cs} \frac{d^2 T_{PEN}}{dz^2} + h_{air} A_{contact} (T_{air} - T_{PEN}) + h_{fuel} A_{contact} (T_{fuel} - T_{PEN}) + \frac{T_{IC} - T_{PEN}}{R_{PEN \leftrightarrow IC}} + q_{rxn} - Q_{NH_3,decomp} = 0 \quad (17)$$

$k_{th,PEN}$ is the thermal conductivity of the PEN

A_{cs} is the cross-sectional area of the PEN

$T_{PEN,i}$ is the local PEN temperature

$h_{air,i}, h_{fuel,i}$ are convective heat transfer coefficients

$T_{air,i}, T_{fuel,i}$ are gas channel temperatures

$R_{PEN \leftrightarrow IC}$ is the interfacial thermal resistance

$q_{rxn,i}$ is the electrochemical heat source

$Q_{NH3,i}$ is the ammonia decomposition heat term

The model architecture treats the PEN and gas channels as separate control volumes that exchange heat through convective heat transfer coefficients defined at their interfaces [29]. Heat transfer coefficients are evaluated locally using the Graetz–Lévêque Nusselt correlation with temperature-dependent transport properties, described in section 2.3.3).

It is assumed that the oxygen reduction reaction and ammonia decomposition contribute to the PEN temperature since these reactions happen inside the cathode and anode respectively, which the model lumps into PEN. Heat generation and consumption calculations for the reactions is outlined in section 2.6).

Associated thermal effects of species consumption and generation are accounted for within the energy balance through reaction source terms. This formulation assumes that product species crossing the PEN-channel interface thermally equilibrate with the bulk channel gas within a single axial segment [29].

Interfacial conduction between the PEN and interconnect is represented using equivalent thermal resistance. The thermal resistance $R_{PEN \leftrightarrow IC}$ accounts for the conductive properties of both materials. Note it is assumed that the PEN and interconnect are in perfect thermal contact where interface contact resistance is considered negligible. We express this as:

$$R_{PEN\leftrightarrow IC} = R_{PEN} + R_{IC} = \frac{t_{PEN}}{k_{PEN}A_{contact,IC\rightarrow PEN}} + \frac{t_{IC}}{k_{IC}A_{contact,IC\rightarrow PEN}} \tag{18}$$

where t_{PEN}, t_{IC} are the PEN an interconnect thicknesses, k_{PEN}, k_{IC} are the thermal conductivities and $A_{contact,IC\rightarrow PEN}$ is the contact area between PEN and interconnect. Heat conduction between the interconnect and PEN is expressed as:

$$\dot{Q}_{PEN\leftrightarrow IC,i} = \frac{T_{IC,i} - T_{PEN,i}}{R_{PEN\leftrightarrow IC}} \tag{19}$$

Implementing equation (17) within the PCFC model requires axial discretization. The second-order temperature derivative in the PEN energy balance is approximated using a finite difference scheme, in which the temperature at each location is expressed in terms of neighboring discretization points.

$$\begin{aligned} k_{th,PEN}A_{cs}\frac{T_{PEN,i-1} - 2T_{PEN,i} + T_{PEN,i+1}}{\Delta z^2} + h_{air,i}A_{contact}(T_{air,i} - T_{PEN,i}) \\ + h_{fuel,i}A_{contact}(T_{fuel,i} - T_{PEN,i}) + \frac{T_{IC,i} - T_{PEN,i}}{R_{PEN\leftrightarrow IC}} + q_{rxn,i} - Q_{NH_3,decomp,i} \\ = 0 \end{aligned} \tag{20}$$

2.3.2) Interconnect energy balance

As stated in section 2.1). the fuel and air side interconnects are represented as a single lumped element. A single energy balance expression would need to capture overall heat transfer mechanisms that the two plates collectively experience. Interconnect heat transfer mechanisms include axial heat conduction, interfacial heat conduction with the PEN

structure, convection with the gas channels as well as ohmic heat generation as the interconnect directs electrons which are released in the PEN electrochemical reactions.

$$k_{th,IC}A_{cs,IC}\frac{d^2T_{IC}}{dz^2} + h_{air,IC}A_{contact,IC}(T_{air} - T_{IC}) + h_{fuel,IC}A_{contact,IC}(T_{fuel} - T_{IC}) + \frac{T_{PEN} - T_{IC}}{R_{IC\leftrightarrow PEN}} + q_{ohm,IC} = 0 \quad (21)$$

The ohmic heat generation within the interconnect is modeled as a resistive loss proportional to the square of the local cell current. The formulation assumes that electrical resistance within the interconnect gives rise to Joule heating, which is distributed over the discretized control volume [18].

$$q_{ohmIC,i} = \frac{{I_{cell,i}}^2 R_{IC}}{dz} \quad (22)$$

$$k_{th,IC}A_{cs,IC}\frac{T_{IC,i-1} - 2T_{IC,i} + T_{IC,i+1}}{\Delta z^2} + h_{air,IC,i}A_{contact,IC}(T_{air,i} - T_{IC,i}) + h_{fuel,IC,i}A_{contact,IC}(T_{fuel,i} - T_{IC,i}) + \frac{T_{PEN,i} - T_{IC,i}}{R_{IC\leftrightarrow PEN}} + q_{ohm,IC,i} = 0 \quad (23)$$

Equation (23) represents the discretized interconnect energy balance based on equation (21)

2.3.3) Fuel and air channel energy balance

Fuel and air channel convective heat transfer mechanisms are captured through local heat transfer coefficients. The coefficients are calculated through empirical correlations such as the Reynolds, Prandtl and Nusselt number. Unlike PEN and interconnect structures where axial conduction requires expressing energy balances through discretized 2nd order ordinary differential relationships, convection only heat transfer in the gas channels enables expressing energy balances as simple algebraic relationships:

$$T_{\text{air},i+1} - T_{\text{air},i} - \frac{h_{\text{air},i} A_{\text{contact,PEN}} \left(T_{\text{PEN},i} - T_{\text{air},i}\right)}{\dot{n}_{\text{tot,air},i}\, c_{p,\text{air},i}} - \frac{h_{\text{air},i} A_{\text{contact},IC} \left(T_{IC,i} - T_{\text{air},i}\right)}{\dot{n}_{\text{tot,air},i}\, c_{p,\text{air},i}} = 0 \tag{24}$$

$$T_{\text{fuel},i+1} - T_{\text{fuel},i} - \frac{h_{\text{fuel},i} A_{\text{contact,PEN}} \left(T_{\text{PEN},i} - T_{\text{fuel},i}\right)}{\dot{n}_{\text{tot,fuel},i}\, c_{p,\text{fuel},i}} - \frac{h_{\text{fuel},i} A_{\text{contact},IC} \left(T_{IC,i} - T_{\text{fuel},i}\right)}{\dot{n}_{\text{tot,fuel},i}\, c_{p,\text{fuel},i}} = 0 \tag{25}$$

Where $h_{\text{air},i}$, $h_{\text{fuel},i}$ are the air and fuel channel heat transfer coefficients and $A_{\text{contact,PEN}}$, $A_{\text{contact},IC}$ are the contact areas per discretized segment between the gas channel and the PEN or interconnect. The specific calculation procedures for the heat transfer coefficient are described below.

The channel volume flows are calculated through the ideal gas law. Species molar flow rates calculated from the mass conservation sub model are added together, representing the total molar flow inside the channel.

$$\dot{n}_{\text{tot},a,i} = \dot{n}_{O_2,i} + \dot{n}_{H_2O,i} + \dot{n}_{N_2,a,i} \tag{26}$$

Where $\dot{n}_{N_2,a,i}$ is the fixed air side nitrogen molar flow rate.

$$\dot{n}_{\text{tot},f,i} = \dot{n}_{H_2,i} + \dot{n}_{N_2,f,i} + \dot{n}_{NH_3,i} \tag{27}$$

Where $\dot{n}_{N_2,f,i}$ is the fuel side nitrogen molar flow rate.

$$\dot{V}_{s,i} = \frac{\dot{n}_{\text{tot},c,i} R T_{s,i}}{P_{\text{cell}}} \tag{28}$$

Where c denotes the fuel of air channel. The volumetric flow rate is divided by the cross-sectional area of the channel to calculate the stream velocity:

$$u_{s,i} = \frac{\dot{V}_{c,i}}{A_{\text{cs},c}} \tag{29}$$

To accurately capture convective heat transfer mechanisms, the gas streams molar masses need to account for multiple species with axially evolving concentrations.

$$\bar{M}_{a,i} = y_{O_2,i} M_{O_2} + y_{N_2,i} M_{N_2} + y_{H_2O,i} M_{H_2O} \tag{30}$$

$$\bar{M}_{f,i} = y_{H_2,i} M_{H_2} + y_{N_2,i} M_{N_2} + y_{NH_3,i} M_{NH_3} \tag{31}$$

Where $y_{\mathrm{k},i}$ represents the species molar fractions expressed as:

$$y_{k,i} = \frac{\dot{n}_{k,i}}{\dot{n}_{\mathrm{tot},i}} \tag{32}$$

The gas stream densities are expressed as:

$$\rho_{c,i} = \frac{P_{\mathrm{cell}} \bar{M}_{c,i}}{R T_{c,i}} \tag{33}$$

On the other hand, the mixture viscosity is expressed as a temperature dependent empirical linear relationship based on outputs from Aspen HYSYS.

$$\mu_{a,i} = \left(0.0000273829\ T_{a,i} + 0.0179576572\right) \times 10^{-3} \tag{34}$$

$$\mu_{f,i} = \left(0.0000235427\ T_{f,i} + 0.0133115641\right) \times 10^{-3} \tag{35}$$

The relationships are approximate since they are evaluated at constant species molar fractions, (0.1 NH_3, 0.3 N_2, 0.6 H_2) for the fuel side and (0.2 O_2, 0.2 H_2O, 0.6 N_2) for the air side. These values are chosen as approximate average molar fractions throughout the cell length.

Similar methodology has been used to calculate the thermal conductivity of the mixtures:

$$k_{th,a,i} = 0.0085678629 + 0.0000699089\ T_{a,i} \tag{36}$$

$$k_{th,f,i} = 0.0455250000 + 0.0001685000\ T_{f,i} \tag{37}$$

Similarly to the mixture molar mass calculation, the stream heat capacities need to account for axially evolving species molar concentrations. Calculation of temperature dependent heat capacities are further explained in section 2.6).

$$c_{p,a,i} = y_{O_2,i} c_{p,O_2,i} + y_{N_2,i} c_{p,N_2,i} + y_{H_2O,i} c_{p,H_2O,i} \tag{38}$$

$$c_{p,f,i} = y_{H_2,i} c_{p,H_2,i} + y_{N_2,i} c_{p,N_2,i} + y_{NH_3,i} c_{p,NH_3,i} \tag{39}$$

The Reynolds number characterizes the flow regime by quantifying the ratio of inertial to viscous forces, thereby influencing the structure of the velocity field.

$$\mathrm{Re}_{c,i} = \frac{\rho_{c,i} u_{c,i} d_{h,c}}{\mu_{c,i}} \tag{40}$$

The Prandtl number relates momentum and thermal diffusivities, indicating the relative thickness of velocity and thermal boundary layers.

$$\mathrm{Pr}_{c,i} = \frac{\mu_{c,i} c_{p,c,i}}{k_{th,c,i}\ \bar{M}_{c,i}} \tag{41}$$

Nusselt number, which represents the dimensionless heat transfer rate and is used to evaluate the local heat transfer coefficient. The Nusselt number equation applied in the model is the Graetz–Lévêque correlation for laminar thermally developing flows for tubular channels [39]. Note that the correlation is developed for tubular channel thermally developing laminar flow while the model cross sectional geometry is square. Using the hydraulic diameter for the square cross section partially accounts for the difference [39].

This is used as an engineering approximation with a ~20% error even in complex geometries and is commonly adopted in previous SOFC modeling papers [39].

Another consideration is that the expression was developed for fully developed parabolic velocity profiles while the current model uses average cross sectional velocity [39]. This introduces an inconsistency between the assumed flow structure and the correlation's theoretical basis. However, given that PCFC channel flows operate at low Reynolds numbers where inertial effects are small and axial transport dominates, the error introduced by this inconsistency is expected to be limited. The Graetz–Lévêque correlation therefore provides a physically reasonable and computationally practical estimate of local heat transfer coefficients within the scope of this model.

$$\mathrm{Nu}_{c,i} = 1.86\left(\frac{\mathrm{Re}_{c,i}\mathrm{Pr}_{c,i}d_{h,c}}{\Delta z}\right)^{1/3} \tag{42}$$

$$h_{s,i} = \frac{\mathrm{Nu}_{c,i}k_{th,c,i}}{d_{h,c}} \tag{43}$$

2.4) PCFC Mass Balance

The mass balance is formulated as a set of discretized algebraic equations representing species molar flow rates along the axial direction of the cell. At each discretized location, the molar flow of each species is updated based on local reaction rates and electrochemical consumption or production. The mass balance model solves four species in total: hydrogen and ammonia at the fuel channel, oxygen and water at the air channel. The main sources of

change in species molar flow rates are the chemical decomposition of ammonia, hydrogen adsorption and subsequent electrochemical oxidation as well as formation of water at the air channel. The general form of mass balance equations is expressed as:

$$\dot{n}_{k,i+1} = \dot{n}_{k,i} + \dot{\omega}_{k,i} \tag{44}$$

where $\dot{n}_{k,i}$and $\dot{n}_{k,i+1}$ are the molar flow rates of species k at axial locations i and $i+1$, respectively, $\dot{\omega}_{k,i}$ is the net molar production or consumption rate of species k within segment i due to chemical and electrochemical reactions.

Equation (44) is next applied in the fuel channel for ammonia, hydrogen and nitrogen and air channel for oxygen and water.

2.4.1) Thermo-catalytic species mass balances

Ammonia molar flow rate is coupled with the ammonia decomposition function introduced by Barat et. al. and further discussed in section 2.5)

$$\dot{n}_{NH_3,i+1} = \dot{n}_{NH_3,i} + RR_{NH_3,i} \tag{45}$$

Where $RR_{NH_3,i}$ represents the ammonia decomposition reaction rate calculated from equation (57).

$$\dot{n}_{N_2,i+1} = \dot{n}_{N_2,i} + \frac{1}{2}\left(\dot{n}_{NH_3,i} - \dot{n}_{NH_3,i+1}\right) \tag{46}$$

Note that nitrogen generation rate is dependent only on the ammonia decomposition kinetics. It does not directly participate in electrochemical reactions since it is electrochemically inert. However, nitrogen influences cell performance indirectly by diluting reactive species in the fuel channel, thereby reducing their partial pressures and contributing to concentration overpotentials Additionally, nitrogen affects thermal and

transport mechanisms through its impact on the fuel channel volume flow rate, heat capacity and density.

The air channel species balances are governed by the electrochemical reactions occurring at the cathode, where oxygen is consumed and water is produced. Nitrogen is treated as an inert species and does not participate in reactions.

2.4.2) Electrochemical species mass balances

Consumption or generation rates of electrochemically active species such as hydrogen, oxygen and water are described through a Faradays law-based formulation, directly linking the molar reaction rates to the local current density. Based on this formulation, the molar rate of species consumption or production is proportional to the local current density and inversely proportional to the number of electrons transferred. Comparing the total current at a segment to the charge carried by electrons involved in the electrochemical reaction enables determining the corresponding amount of reactants participating in the local reaction process. Thus, expressions for each species are based on the stoichiometric relations (2) and (1).

$$R_{k,i}^{\mathrm{el}} = \frac{I_{cell,i}}{Z_k F} \tag{47}$$

Where $R_{k,i}^{\mathrm{el}}$ is the electrochemical reaction rate of species k, $i_{cell,i}$ is the total segment cell current density based on equation (5), n_k is the number of electrons involved in the electrochemical reaction.

There are two mechanisms governing the molar flow rate of hydrogen. Molar flow is increased by the hydrogen produced in the ammonia decomposition reaction while it decreases through electrochemical oxidation.

$$\dot{n}_{H_2,i+1} = \dot{n}_{H_2,i} - \frac{I_{\text{cell},i}}{2 \cdot F} + RR_{H_2,i} \tag{48}$$

Where $Z_k = 2$ based on equation (1)

Oxygen is supplied to the cathode where it is electrochemically reduced, subsequently reacting with hydrogen protons supplied through the electrolyte to produce water described by equation (2). Applying the eq (2) to eq (47) yields the discretized molar flow expressions:

$$\dot{n}_{O_2,i+1} = \dot{n}_{O_2,i} - \frac{I_{\text{cell},i}}{4 \cdot F} \tag{49}$$

Where $Z_k = 4$ correspond to equation (2). The term $\frac{i_{\text{cell},i}}{4 \cdot F}$ is negative as oxygen is consumed to form water. Conversely, the water molar flow rate is expressed as:

$$\dot{n}_{H_2O,i+1} = \dot{n}_{H_2O,i} + \frac{I_{\text{cell},i}}{2 \cdot F} \tag{50}$$

where $Z_k = 2$ correspond to equation (2). The calculated molar flow values are plugged into equation (32) to find the molar fractions of each species. Molar fractions are thus used to calculate the species partial pressures, which are utilized throughout multiple sub models.

$$P_{k,i} = y_{k,i} = \frac{\dot{n}_{k,i}}{\dot{n}_{\text{tot},i}} \cdot P_{cell} \tag{51}$$

2.5) Ammonia Decomposition Kinetics

The direct electrochemical oxidation of ammonia is both kinetically and thermodynamically unfavorable, indicating that ammonia utilization proceeds predominantly through catalytic decomposition to hydrogen which subsequently reacts electrochemically [40], [41]. Ammonia decomposition is commonly expressed through the stoichiometric equation:

$$\mathrm{NH_3} \rightarrow \frac{1}{2}\mathrm{N_2} + \frac{3}{2}\mathrm{H_2} \tag{52}$$

While this equation captures the overall relationship between the reactants and products, it does not describe the catalytic processes that govern the reaction kinetics under system operating conditions. Ammonia decomposition is a complex 6-step mechanism outlined in Table 1)

Table 1 Ammonia six step decomposition mechanism

Step 1	$\mathrm{NH_3} + * \rightleftharpoons \mathrm{NH_3^*}$
Step 2	$\mathrm{NH_3^*} + * \rightleftharpoons \mathrm{NH_2^*} + \mathrm{H^*}$
Step 3	$\mathrm{NH_2^*} + * \rightleftharpoons \mathrm{NH^*} + \mathrm{H^*}$
Step 4	$\mathrm{NH^*} + * \rightleftharpoons \mathrm{N^*} + \mathrm{H^*}$
Step 5	$2\mathrm{N^*} \rightleftharpoons \mathrm{N_2} + 2*$
Step 6	$2\mathrm{H^*} \rightleftharpoons \mathrm{H_2} + 2*$

While the ammonia decomposition is thermodynamically favorable at the operating temperatures of a PCFC, sluggish reaction kinetics require introducing catalysts to decrease the activation energy and increase the reaction rate [42], [43], [44]. Ammonia molecules adsorb at the active catalyst sites in the anode structure marked by * sign and dissociate as the catalyst lowers the activation energy required to break the N-H bonds. The

dissociation rate is limited by the amount of active catalyst sites, often expressed through the active catalyst surface area per anode volume [16], [45].

During operation, catalyst surface sites are dynamically occupied by adsorbed intermediates such as NH_3, NH_2, NH, N, and H. The relative rates of elementary steps determine the varying coverages of each species. Sites are freed as adsorbed N atoms recombine and desorb as N_2 and adsorbed H atoms recombine and desorb as H_2, making these desorption steps critical to maintaining catalytic activity [43], [44], [45].

In addition, the reaction kinetics are governed by the presence of gas phase species. Higher partial pressure of ammonia increases the chances that the molecules are adsorbed at a catalyst, increasing the reaction rate [43], [45]. On the other hand, higher partial pressures of hydrogen cause hydrogen to accumulate at the active sites, inhibiting ammonia from reacting and limiting the overall reaction rate [43], [45].

A fully developed model would solve surface coverage ODEs for each intermediate adsorbed species at every anode segment in addition to gas phase species balances. Solving for the full six step ammonia decomposition mechanism may be inadequate for system level modeling due to high computational requirements and increased model stiffness.

A simplified Langmuir-Hinshelwood based expression represents a viable alternative. Barat utilizes validated six step experimental reaction rate data published by Okura for a Ni-BaZrO3 electrode to develop a simple two-parameter rate expression for NH3 decomposition. This approach enables accurate simulation of ammonia decomposition

while being comparatively less numerically stiff. The expression is derived under the assumption that nitrogen recombination is the rate limiting step while other steps are in fast equilibrium [40], [45].

Note that the model is valid for a 650 – 950 K temperature range which is inside the upper operating bounds of the model. The rates are calibrated under a pressure of $1 \cdot 10^5\ Pa$ [45]. The expression was validated for both pure ammonia and ammonia-hydrogen-nitrogen mixtures which reflect the species compositions inside the PCFC model [45].

The ammonia decomposition kinetics model is developed based on experimental data obtained for $\mathrm{Ni} - \mathrm{BaZrO_3}$ anodes, due to the limited availability of kinetic models specifically parameterized for Ni–BCZYYb systems. This assumption reflects the approach by Zhu et al. in the multi-step ammonia decomposition model, where $\mathrm{Ni} - \mathrm{BaZrO_3}$ data were used as a representation of Ni–BCZYYb electrodes. According to Zhu et al [16], the $\mathrm{Ni} - \mathrm{BaZrO_3}$ system represents the closest available analogue in terms of electrode structure and catalytic behavior, and the kinetic parameters were adjusted to capture the dominant catalytic effects, even though support-specific interactions are not explicitly represented.

$$r_{\mathrm{NH_3}} = -\frac{k_{\mathrm{NH_3}}\, P_{\mathrm{NH_3}}^2}{\left(P_{\mathrm{H_2}}^{3/2} + \hat{k}_{\mathrm{NH_3}} P_{\mathrm{NH_3}}\right)^2} \tag{53}$$

Where $r_{\mathrm{NH_3}}$ is the intrinsic ammonia reaction rate, $k_{\mathrm{NH_3}}$ is the kinetic rate constant, $\hat{k}_{\mathrm{NH_3}}$ is the hydrogen inhibition coefficient and $P_{\mathrm{NH_3}}, P_{\mathrm{H_2}}$ are the partial pressures of ammonia and

hydrogen respectively. Kinetic rate constant k describes the intrinsic speed of the chemical reaction on the catalyst surface at a given temperature.

$$\ln\left(k_{\mathrm{NH_3}}\right) = a_k + b_k\left(\frac{1}{T_{\mathrm{PEN}}}\right) + c_k\left(\frac{1}{T_{\mathrm{PEN}}}\right)^2 \tag{54}$$

Hydrogen inhibition coefficient $\hat{k}$ represents the competitive adsorption between hydrogen and ammonia on the anode catalyst surface. It is expressed as:

$$\ln\left(\hat{k}_{\mathrm{NH_3}}\right) = a_{\hat{k}} + b_{\hat{k}}\left(\frac{1}{T_{\mathrm{PEN}}}\right) + c_{\hat{k}}\left(\frac{1}{T_{\mathrm{PEN}}}\right)^2 \tag{55}$$

Where $a_{\hat{k}}$, $b_{\hat{k}}$, $c_{\hat{k}}$ are the fitted coefficients which are taken from Barat [45]:

Table 2 Ammonia decomposition kinetics parameters

Coefficient	$k_{\mathrm{NH_3}}\left(\frac{mol \cdot Pa}{s * m\text{^}2}\right)$	$\hat{k}_{\mathrm{NH_3}}\left(\sqrt{Pa}\right)$
a	-5.996	-6.181
b	$4.344 \cdot 10^4$	$2.849 \cdot 10^4$
c	$-2.610 \cdot 10^7$	$-1.287 \cdot 10^7$

Before plugging in the computed expressions (54) and (55), we use:

$$k_{\mathrm{NH_3}} = e^{\ln k_{\mathrm{NH_3}}}, \hat{k}_{\mathrm{NH_3}} = e^{\ln \hat{k}_{\mathrm{NH_3}}} \tag{56}$$

This expression converts the fitted logarithmic expressions back into actual physical parameters. Finally, to find the reaction rate at segment i we multiply the intrinsic reaction rate $r_{\mathrm{NH_3}}$ with the total catalyst area per anode segment volume.

$$RR_{NH_3} = r_{NH_3} \cdot A_{cat} \cdot A_{cs} \cdot dz \tag{57}$$

Where A_{cat} is the catalyst area per bed volume, A_{cs} is the cross-sectional area of the anode and dz is the segment length. As the ammonia is dissociated, hydrogen and nitrogen molecules are released into the fuel channel. The product amounts are determined by the stoichiometric relationship (52).

$$RR_{H_2} = \frac{3}{2} \cdot RR_{NH_3} \tag{58}$$

$$RR_{N_2} = \frac{1}{2} \cdot RR_{NH_3} \tag{59}$$

Under the conditions of the Barat paper, adsorbed N atoms are assumed to be the dominant surface species, meaning N atom recombination (Step 5) is both the rate limiting step and the primary determinant of available vacant sites. Nickel is commonly utilized in ammonia fed fuel cells because of its performance and lower cost [44]. Barat utilizes reaction rate data generated from a validated six-step elementary mechanism (itself calibrated against Okura et al. [43] experimental data for a Ni-$BaZrO_3$ catalyst) to derive and calibrate a simplified two-parameter Langmuir-Hinshelwood rate expression for NH_3 decomposition, enabling engineering-level reactor calculations without requiring a detailed mechanism solver.

2.6) Thermochemical Properties

Accurate representation of temperature-dependent thermodynamic properties such as species heat capacities, enthalpies, Gibbs free energy, and reaction enthalpy changes requires the use of fitted correlations. In this work, the temperature dependence of these properties is described using the Shomate equations provided in the NIST Chemistry Webbook database [46].

Note that each species has multiple sets of Shomate parameters that are valid for distinct temperature sub-ranges. However, introducing conditional statements selecting the parameter sets based on the local species temperature introduces discontinuities in variable behavior. This is incompatible with the utilized Newton type solver due to introduced discontinuities as discussed in section 2.8).

$$C_p^\circ = A + Bt + Ct^2 + Dt^3 + \frac{E}{t^2} \tag{60}$$

$$H^\circ - H_{298.15}^\circ = At + \frac{Bt^2}{2} + \frac{Ct^3}{3} + \frac{Dt^4}{4} - \frac{E}{t} + F - H \tag{61}$$

$$S^\circ = A\ln(t) + Bt + \frac{Ct^2}{2} + \frac{Dt^3}{3} - \frac{E}{2t^2} + G \tag{62}$$

Where $C_p^\circ$is the molar heat capacity (J mol^{-1} K^{-1}), $H^\circ$is the molar enthalpy (kJ mol^{-1}), $S^\circ$is the molar entropy (J mol^{-1} K^{-1}), and $t = T/1000$. Temperature T is taken to be the fuel or air channel temperature depending on the species location. The parameters for Shomate expressions differ for various temperature ranges, with exact parameters being chosen to fit into the operating temperature ranges of the cell.

Table 3 Implemented Shomate Parameters

Parameter	NH_3 (298–1400 K)	N_2 (500–2000 K)	H_2 (298–1000 K)	H_2O (500–1700 K)	O_2 (700–2000 K)
A	19.99563	19.50583	33.06618	30.092	30.03235
B	49.77119	19.88705	-11.3634	6.832514	8.772972
C	-15.376	-8.59854	11.43282	6.793435	-3.98813
D	1.921168	1.369784	-2.77287	-2.53448	0.788313
E	0.189174	0.527601	-0.15856	0.082139	-0.7416

F	-53.3067	-4.9352	-9.9808	-250.881	-11.3247
G	203.8591	212.39	172.708	223.3967	236.1663
H	-45.8981	0	0	-241.826	0

$H^\circ - H^\circ_{298.15}$ represents sensible enthalpy relative to 298 K reference temperature, accounting for the enthalpy temperature dependence. However, sensible enthalpy is insufficient to fully describe chemical reactions. Thus, the formation enthalpy term is introduced to account for the change in enthalpy from the broken and formed bonds during a chemical reaction per mole of reacting species. The total change in enthalpy of a chemical reaction is described as:

$$H^\circ(T) = H_f^\circ + (H^\circ(T) - H^\circ_{298.15}) \tag{63}$$

By convention, the formation enthalpy of $H_2O_2N_2$ is taken as 0. The formation enthalpies of ammonia and water are taken as: -45.94 kJ/mol and -241.8264 kJ/mol respectively [46]. The overall change in enthalpy of a chemical reaction is defined as the difference of product and reactant species enthalpy changes:

$$\Delta H_{\mathrm{rxn},i} = \sum_{\text{products}} \nu_j \ \Delta H_{j,i} - \sum_{\text{reactants}} \nu_k \ \Delta H_{k,i} \tag{64}$$

where $\Delta H_{\mathrm{rxn},i}$is the reaction enthalpy at axial location i, ν represents the stoichiometric coefficients of the participating species, and $\Delta H_{j,i}$and $\Delta H_{k,i}$denote the molar enthalpies of the product and reactant species, respectively.

Applying equation (64) to reactions (2) (52) yields:

$$\Delta H_{\mathrm{ORR},i} = \Delta H_{H_2O,i} - \Delta H_{H_2,i} - \frac{1}{2}\Delta H_{O_2,i} \tag{65}$$

$$\Delta H_{\mathrm{NH_3,dec},i} = \frac{3}{2}\Delta H_{H_2,i} + \frac{1}{2}\Delta H_{N_2,i} - \Delta H_{NH_3,i} \tag{66}$$

The change in entropy of the oxygen reduction reaction is similarly computed:

$$\Delta S_{\mathrm{rxn},i} = \sum_{\text{products}} \nu_j \ \Delta S_{j,i} - \sum_{\text{reactants}} \nu_k \ \Delta S_{k,i} \tag{67}$$

Where $\Delta S_{j,i}$ is the reaction entropy at axial location i and $\Delta S_{j,i}$ and$\Delta S_{k,i}$ denote the molar entropies of the product and reactant species, respectively.

$$\Delta S_{\mathrm{ORR},i} = \Delta S_{H_2O,i} - \Delta S_{H_2,i} - \frac{1}{2}\Delta S_{O_2,i} \tag{68}$$

$$\Delta S_{\mathrm{NH_3,dec},i} = \frac{3}{2}\Delta S_{H_2,i} + \frac{1}{2}\Delta S_{N_2,i} - \Delta S_{NH_3,i} \tag{69}$$

In a fuel cell, Gibbs free energy describes the maximum electrical work that can be delivered at constant operating pressure and temperature [47]. Gibbs energy of the ORR governs the maximum theoretical potential and electrochemical cell behavior through the Nernst potential as seen in equation (6). With computed reaction enthalpies and entropies, we can determine the reaction Gibbs energy as:

$$\Delta G_{\mathrm{ORR},i} = \Delta H_{\mathrm{ORR},i} \times 1000 - T_{\mathrm{PEN},i}\ \Delta S_{\mathrm{ORR},i} \tag{70}$$

$$\Delta G_{\mathrm{NH_3},i} = \Delta H_{\mathrm{NH_3},i} \times 1000 - T_{\mathrm{PEN},i}\ \Delta S_{\mathrm{NH_3,dec},i} \tag{71}$$

Note that the Shomate equations yield $\frac{kJ}{mol}$ for $\Delta H_{\mathrm{rxn},i}$ and $\frac{J}{mol \cdot K}$ for $\Delta S_{\mathrm{rxn},i}$. $\Delta H_{\mathrm{rxn},i}$ is accordingly multiplied by a factor of 1000 to express Gibbs free energy in terms of $\frac{J}{mol}$. The model uses the lumped $T_{\mathrm{PEN},i}$ as we assume that the reacting species temperatures reach the same temperature as the porous electrode.

2.7) Model Parameters

2.7.1) Geometric parameters

Table 4 Geometric Parameter Overview

Parameter	Symbol	Value	Units	Description	Source
Number of axial segments	N	60	-	Number of discretized control volumes along flow direction	
Channel length	$L_{channel}$	0.1	m	Total axial length of the fuel cell channel	[48]
Segment length	Δz	L/N	m	Length of each discretized segment	
Total active area	$A_{\mathrm{active,total}}$	0.0081	m^2	Total electrochemically active area of the cell	[48]
Segment active area	A_{active}	A_total/N	m^2	Active area per axial segment	
Total contact area	$A_{\mathrm{contact,total}}$	0.75*A_active,total	m^2	Heat/mass transfer interface area	[18]
Segment contact area	A_{contact}	A_contact,total/N	m^2	Contact area per segment	
PEN cross-sectional area	A_{cs}	$5.2 \cdot 10^{-5}$	m^2	Cross-sectional area used in conduction calculations ($\tau_{PEN} \cdot 0.1$)	
Fuel channel	$A_{\mathrm{cs,fuel}}$	Derived	m^2	Effective fuel channel flow area	

cross-section					
Air channel cross-section	$A_{\mathrm{cs,air}}$	Same as fuel	m^2	Effective air channel flow area	
Hydraulic diameter (air)	$d_{h,air}$	0.005	m	Hydraulic diameter for air channel	[23]
Hydraulic diameter (fuel)	$d_{h,fuel}$	0.005	m	Hydraulic diameter for fuel channel	[23]
Interconnect cross-section	$A_{\mathrm{cs,IC}}$	$6.5 \cdot 10^{-4} \cdot 0.1$	m^2	Cross-sectional area for IC conduction	
Interconnect contact area	$A_{\mathrm{contact,IC}}$	$0.25 \cdot A_{\mathrm{contact}}$	m^2	Contact area between IC and fluids	
Interconnect thickness	τ_{IC}	$6.5 \cdot 10^{-4}$	m	Thickness of interconnect plate	[18]
PEN thickness	τ_{PEN}	$(485+15+20) \cdot 10^{-6}$	m	Total PEN thickness	[49]
Catalyst surface area density	A_{cat}	$4 \cdot 10^{6}$	m^{-1}	Effective catalytic surface per unit volume	[45]
Anode thickness	τ_{an}	$485 \cdot 10^{-6}$	m	Anode thickness used for TPB species pressure calculation	[49]
Cathode thickness	τ_{ca}	$20 \cdot 10^{-6}$	m	Cathode thickness used for TPB species pressure calculation	[49]

The dimensional values are typical for a 0.1 x 0.1 m planar fuel cell. 75 % of the PEN surface area is spanned by gas channels expressed as total contact area, while 25% is spanned by the interconnect structure expressed as interconnect contact area. The gas channel has a 0.005 x 0.005 mm cross section. As the channels are square the hydraulic diameter is calculated as the length of the side.

The PEN cross sectional area is calculated as a sum of anode, electrolyte and cathode thicknesses times the width of the fuel cell.

$$A_{cs,PEN} = (\tau_{anode} + \tau_{electrolyte} + \tau_{cathode}) \cdot 0.1 \; = \; (485 + 15 + 20) \cdot 10^{-6} \cdot 0.1$$

The model is discretized into 60 points. To find dimensionally consistent values used for calculations at each discretized point, values such as total active and contact areas are divided by the number of points to find per segment areas.

2.7.2) Other parameters

Representative model outputs require the selection of parameters consistent with a specific anode, cathode, electrolyte, and interconnect material system. The developed PCFC model considers barium cerate zirconate co-doped with yttria (BCZY) as the electrolyte material. It should be noted that even within the same electrolyte class, operational parameters may vary depending on fabrication methods and specific co-dopant compositions. BCZY was chosen as a commonly implemented material with a large scope of publications providing performance data. Ni-BaZrO3 represents the anode material. This material was used by Okura in experimental ammonia decomposition study which Barat used to develop the ammonia decomposition rate expression. Electrochemical parameters are sourced from multiple modeling and experimental studies. The model consists of 12 independent adjustable input parameters. It is assumed that all species present in the air and fuel channels have equal temperatures. Certain conducted parametric studies express mass flow rates as average cell current density dependent values (90), reducing the number of

independent inputs to 6. In addition, model is most accurate at atmospheric pressure since it reflects the conditions Barat used to for ammonia decomposition kinetics parameters

Table 5 Independent Adjustable Inputs

Parameter	Units	Parameter	Units
$j_{cell,in}$	$\frac{A}{m^2}$	$\dot{m}_{O2,in}$	$\frac{kg}{s}$
P_{cell}	Pa	$\dot{m}_{H2O,in}$	$\frac{kg}{s}$
$T_{PEN,in}$	K	$\dot{m}_{NH3,in}$	$\frac{kg}{s}$
$T_{IC,in}$	K	$\dot{m}_{N2,in,fuel}$	$\frac{kg}{s}$
$T_{air,in}$	K	$\dot{m}_{N2,in,air}$	$\frac{kg}{s}$
$T_{fuel,in}$	K	$\dot{m}_{H2,in}$	$\frac{kg}{s}$

Table 6 Conductivity and Diffusivity Parameters

Parameter	Value	Units	Reference
k_{IC}	24	$\frac{W}{m \cdot K}$	[18]
k_{PEN}	2	$\frac{W}{m \cdot K}$	[18]
D_{an}	$3 \cdot 10^{-5}$	$\frac{m^2}{s}$	[18]
D_{ca}	$3 \cdot 10^{-6}$	$\frac{m^2}{s}$	[18]

2.8) Solver Architecture

Ammonia decomposition kinetics are described by an expression introduced by Barat et.al. which is further described in section 2.5). Note that the depletion of ammonia needs to be

constrained to maintain the partial pressure in a non-negative range. The constraint is implemented using a maximum function, which enforces a lower bound by selecting the higher value between the computed ammonia partial pressure and a specified threshold value.

$$if\ P_{NH_3,i} > lower\ boundary\ \rightarrow\ P_{NH_3,i} = P_{NH_3,i} \qquad (72)$$
$$if\ P_{NH_3,i} < lower\ boundary\ \rightarrow\ P_{NH_3,i} = 0$$

The maximum function described in equation (72) introduces discontinuity in the Newton solver, causing convergence failure as the Jacobian becomes unreliable near the boundary. The discontinuous transition at the point where ammonia is depleted needs to be approximated using a continuous function. A continuous function which mimics the behavior of equation (72) is represented as:

$$P_{NH3} = \frac{1}{2}\left(P_{NH3} + \sqrt{{P_{NH3}}^2 + \varepsilon_{p,NH3}^2}\right) \qquad (73)$$

This prevents the model from diverging when ammonia is depleted. The model addresses this by utilizing a hyperbolic tangent smoothing function. The $\tanh(\cdot)$function is a smooth, continuous, and differentiable sigmoidal function that transitions monotonically between -1 and $+1$. It is approximately linear near the origin and gradually saturates toward its asymptotic limits for large positive and negative inputs. This behavior enables a smooth approximation of sharp transitions, replacing discontinuous switching with a continuous transition region while preserving numerical stability.

$$a \cdot tanh(b \cdot x + c) + d \quad (74)$$

The hyperbolic tangent function will multiply the computed ammonia decomposition by a factor of 1 as it reaches unity at positive NH3 partial pressure. As the partial pressure of ammonia reaches 0, the tanh function will decrease and reach its lower asymptotic limit of 0, suppressing the reaction rate. To achieve this behavior, appropriate scaling parameters need to be chosen. In addition, the transition between the upper and lower function limits can still prevent convergence if the transition is too sharp. On the other hand, an overly gradual transition will introduce a premature decrease of the reaction rate, introducing nonphysical behavior in the model.

$$0.5 \cdot tanh(50 \cdot x - 50) + 0.5 \quad (75)$$

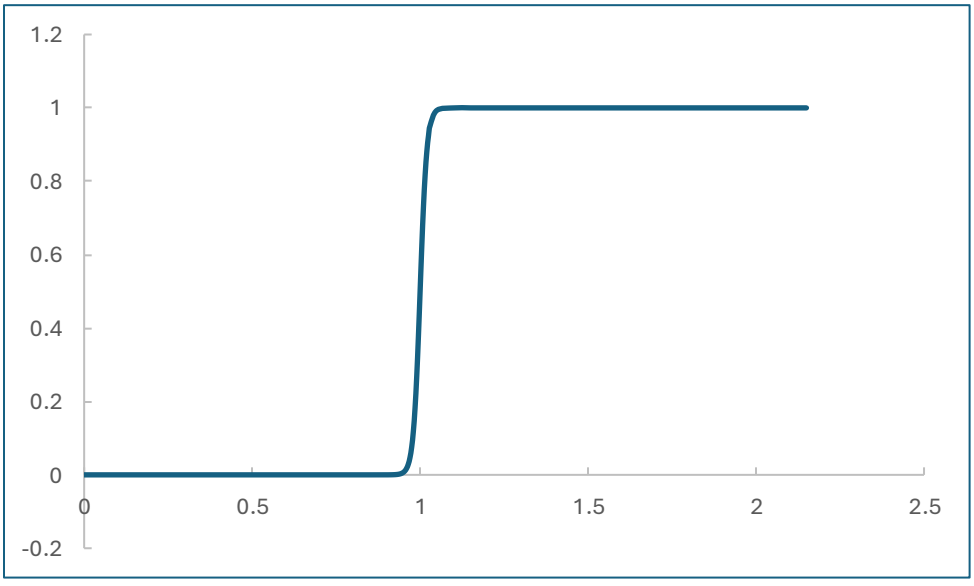

Figure 5 tanh smoothing function adopted in the ammonia decomposition submodel

An approach analogous to hyperbolic tangent smoothing has been applied to the electrochemical submodel to ensure numerical stability under fuel-depleted conditions.

During operation, as the hydrogen partial pressure at the triple phase boundary (TPB) approaches zero, the logarithmic dependence in the Nernst potential and concentration overpotential formulations introduces strong nonlinearities. More specifically, the Nernst potential decreases sharply due to its dependence on $\ln(p_{H_2})$, while the concentration overpotential increases significantly because of transport limitations at the TPB.

Another dependent electrochemistry term is the concentration overpotential where reduced hydrogen pressure increases the logarithmic term $\ln\left(\frac{p_{H_2,\text{bulk}}}{p_{H_2,\text{TPB}}}\right)$ which is proportional to η_{conc}. These effects reflect fuel starvation as the decrease in availability of hydrogen in electrochemical reactions reduces the maximum operating capacity and concentration overpotential. Consequently, to satisfy equation (3), the system needs to decrease the cell current density output. However, the direct evaluation of these logarithmic terms leads to numerical singularities as $p_{H_2,\text{TPB}} \to 0$, resulting in instability in nonlinear solvers. Hence, a smoothing function is introduced, preventing non-physical divergence while preserving the asymptotic trend of current collapse under fuel-limited conditions. This approach reduces model stiffness and enables convergence at boundary operating conditions. Note that this might have an impact on result accuracy depending on implementation, hence requiring detailed validation in section 3.1). The approach requires adjusting the input pressure values to be slightly above zero at hydrogen depletion as well as limiting the reactant levels in a positive range. Two mechanisms are introduced to improve convergence. A modified max function is introduced into the electrochemical partial pressure terms.

$$P^{safe} = \frac{1}{2}\left(P + \sqrt{P^2 + \varepsilon_p^2}\right) \tag{76}$$

$$P_{k,TPB}^{safe} = \frac{1}{2}\left(P_{k,TPB} + \sqrt{P_{k,TPB}^2 + \varepsilon_p^2}\right) \tag{77}$$

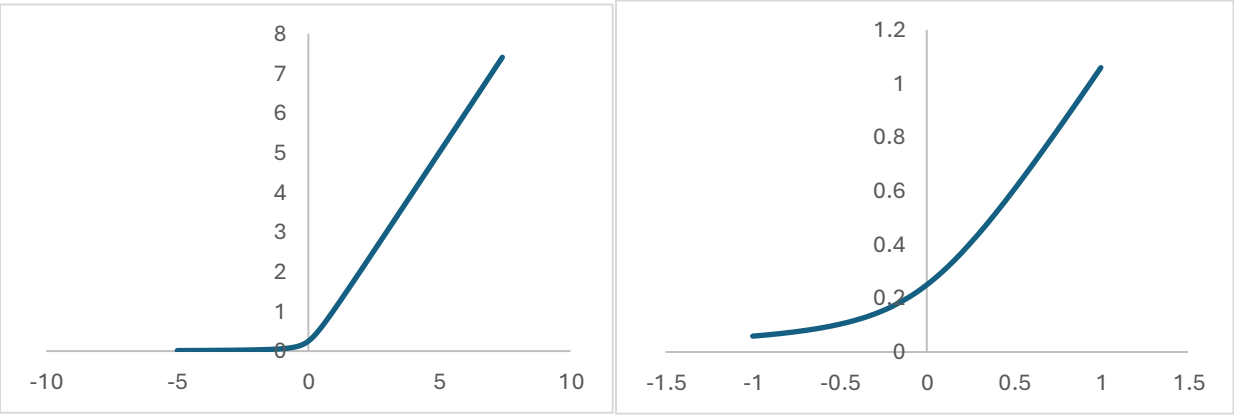

Figure 6 continuous max function (left) with detailed behavior at zero (right)

Implementing equation (77) reduces the risk of divergence introduced by max function discontinuity. Additionally, it prevents the Nernst and concentration overpotential terms from reaching infinity by approximating P=0 as P=0.2 which prevents it from diverging.

Another step to ensuring physical results is a hyperbolic tangent function in the mass balance sub model. The driving force of hydrogen consumption is the cell current density which may still overshoot hydrogen levels into negative values. Multiplying the entire expression with a hyperbolic function may cause model divergence. Instead, the hyperbolic tangent function multiplies the current density consumption term, ensuring better stability. The function is designed to switch from its upper boundary to the lower boundary (1 – 0) when the hydrogen reaches a specified threshold, preventing any further consumption.

Electrochemistry

The PEN, interconnect, and channel energy balances are solved as a coupled system, where temperature-dependent properties and heat transfer terms link the individual sub models. PEN energy balance is described by a nonlinear steady state second order ODE representing 1-D heat conduction. PEN solver arranges the discretized equations into the coefficient matrix for PEN temperature dependent terms and source matrix for independent terms, forming a system of algebraic equations.

$$A\mathbf{x} - \mathbf{b} = 0 \tag{78}$$

where $A$is the coefficient matrix arising from the discretized PEN energy balance, $\mathbf{x}$is the vector of unknown PEN temperatures at the discretized axial locations, and $\mathbf{b}$is the source vector containing the independent terms, including convective contributions and heat generation or consumption terms. Because several coefficients in Adepend on temperature-dependent properties, the system is nonlinear, even though it is written in matrix form. The discretized formulation determines the temperature at each node as a function of its neighboring points, ensuring smooth temperature behavior along the axial direction.

$$k_{PEN}A_{cs}\frac{T_{i-1} - 2T_i + T_{i+1}}{\Delta z^2} + h_{air,i}A_{contact}(T_{air,i} - T_i) + h_{fuel,i}A_{contact}(T_{fuel,i} - T_i) + \frac{T_{IC,i} - T_i}{R_{PEN\leftrightarrow IC}} + q_{rxn,i} - Q_{NH_3,i} = 0 \tag{79}$$

Referring to equation (79), the discretized PEN energy balance at each axial location involves temperature terms from the neighboring points $i-1$, i, and $i+1$. This coupling is reflected

in the tridiagonal structure of the coefficient matrix A. Rearranging equation (79) to isolate the terms multiplying the unknown temperatures from the independent source terms yields:

$$\left(\frac{k_{PEN}A_{cs}}{\Delta z^2}\right)T_{i-1} + \left(\frac{2k_{PEN}A_{cs}}{\Delta z^2} - h_{air,i}A_{contact} - h_{fuel,i}A_{contact} - \frac{1}{R_{PEN\leftrightarrow IC}}\right)T_i + \left(\frac{k_{PEN}A_{cs}}{\Delta z^2}\right)T_{i+1} + h_{air,i}A_{contact}T_{air,i} + h_{fuel,i}A_{contact}T_{fuel,i} + \frac{T_{IC,i}}{R_{PEN\leftrightarrow IC}} + q_{rxn,i} - Q_{NH_3,i} = 0 \quad (80)$$

The matrix sizes are NxN, Nx1 and Nx1 for the A, b, and x matrices respectively. The matrices are populated accordingly based on equation (80). Energy balance is applied over the index range $i = 1$ to $N - 2$, corresponding to interior discretization points, while the boundary nodes are excluded to allow the enforcement of prescribed boundary conditions. To solve the system, appropriate boundary conditions must be defined for both the inlet and the outlet. Dirichlet boundary condition states that the PEN temperature matches the temperature of a strong heat reservoir at the boundary, which is appropriate for the specified inlet fuel cell temperatures.

$$T_{PEN,0} = T_{inlet} \quad (81)$$

While appropriate for the inlet, this condition may be inappropriate at the outlet, where the temperature is not known a priori and is instead governed by the internal energy balance of the system. Alternatively, the system can be constrained by a specified heat flux at the boundary, also known as the Neumann condition. Since the system was previously characterized as adiabatic, it can be specified that no heat leaves the PEN at the outlet based on equation:

$$\frac{T_N - T_{N-1}}{\Delta z} = 0 \Rightarrow T_N = T_{N-1} \tag{82}$$

Overall, the solver is structured as follows:

$$0 = \begin{bmatrix} 1 & 0 & 0 & 0 & \cdots & 0 \\ a_1 & d_1 & c_1 & 0 & \cdots & 0 \\ 0 & a_2 & d_2 & c_2 & \cdots & 0 \\ 0 & 0 & a_3 & d_3 & \cdots & 0 \\ \vdots & \vdots & \vdots & \ddots & \ddots & c_{N-2} \\ 0 & 0 & 0 & \cdots & -1 & 1 \end{bmatrix} * \begin{bmatrix} T_{PEN,0} \\ T_{PEN,1} \\ T_{PEN,2} \\ \vdots \\ T_{PEN,N-2} \\ T_{PEN,N-1} \end{bmatrix} - \begin{bmatrix} T_{left} \\ b_{PEN,1} \\ b_{PEN,2} \\ b_{PEN,3} \\ \vdots \\ 0 \end{bmatrix} \tag{83}$$

where:

$$a_i = \frac{k_{PEN} A_{cs}}{\Delta z^2}\ , c_i = \frac{k_{PEN} A_{cs}}{\Delta z^2}\ , d_i = -\frac{2k_{PEN} A_{cs}}{\Delta z^2} - h_{air,i} A_{contact} - h_{fuel,i} A_{contact} - \frac{1}{R_{PEN \leftrightarrow IC}} \tag{84}$$

$$b_{PEN,i} = h_{air,i} A_{contact} T_{air,i} + h_{fuel,i} A_{contact} T_{fuel,i} + \frac{T_{IC,i}}{R_{PEN \leftrightarrow IC}} + q_{rxn,i} - Q_{NH_3,decomp,i} \tag{85}$$

The numerical solver iterates through different PEN temperature profiles to find an array of values for which the residual function in every matrix row each yields 0.

Since heat transfer mechanisms of the interconnect structure are similar to the PEN, same solver structure is applied. The discretized energy balance applied for the solver matrices is expressed as:

$$k_{IC} A_{cs,IC} \frac{d^2 T_{IC}}{dz^2} + h_{air,IC} A_{contact,IC} (T_{air} - T_{IC}) + h_{fuel,IC} A_{contact,IC} (T_{fuel} - T_{IC}) + \frac{T_{PEN} - T_{IC}}{R_{IC \leftrightarrow PEN}} + q_{ohm,IC} = 0 \tag{86}$$

The interconnect boundary conditions reflect the ones set for the PEN structure. Discretizing the interconnect energy balance equation and expressing the formulation in matrix form yields:

$$0 = \begin{bmatrix} 1 & 0 & 0 & 0 & \cdots & 0 \\ a_1^{IC} & d_1^{IC} & c_1^{IC} & 0 & \cdots & 0 \\ 0 & a_2^{IC} & d_2^{IC} & c_2^{IC} & \cdots & 0 \\ 0 & 0 & a_3^{IC} & d_3^{IC} & \cdots & \vdots \\ \vdots & \vdots & \vdots & \ddots & \ddots & c_{N-2}^{IC} \\ 0 & 0 & 0 & \cdots & -1 & 1 \end{bmatrix} \begin{bmatrix} T_{IC,0} \\ T_{IC,1} \\ T_{IC,2} \\ \vdots \\ T_{IC,N-2} \\ T_{IC,N-1} \end{bmatrix} - \begin{bmatrix} T_{IC,left} \\ b_{IC,1} \\ b_{IC,2} \\ b_{IC,3} \\ \vdots \\ 0 \end{bmatrix} \quad (87)$$

where:

$$a_i^{IC} = \frac{k_{IC} A_{cs,IC}}{\Delta z^2}, c_i^{IC} = \frac{k_{IC} A_{cs,IC}}{\Delta z^2} \quad (88)$$

$$d_i^{IC} = -\frac{2k_{IC} A_{cs,IC}}{\Delta z^2} - h_{air,IC,i} A_{contact,IC} - h_{fuel,IC,i} A_{contact,IC} - \frac{1}{R_{IC \leftrightarrow PEN}}$$

$$b_{IC,i} = h_{air,IC,i} A_{contact,IC} T_{air,i} + h_{fuel,IC,i} A_{contact,IC} T_{fuel,i} + \frac{T_{PEN,i}}{R_{IC \leftrightarrow PEN}} + q_{ohm,IC,i} \quad (89)$$

For the fuel and air channels, the model assumes convection heat transfer only. This simplifies the solver structure since the behavior can be described using algebraic relations without requiring the solution of differential energy equations. To solve the discretized expression, only an inlet boundary condition needs to be defined.

Overall, the system has 4N residual functions, where the PEN and interconnect solver have two enforced conditions each while the gas channels have one. Hence, the energy balance sub model solves for 234 (4N-6) residual equations in total.

Mass balance:

Mass balance is structurally simplest, with a set of algebraic residual functions describing the molar flows of species at every discretized point. The model solves four species in total: hydrogen and ammonia for the fuel channel, oxygen and water at the air channel. Note that

even though it is present in channel flows, nitrogen is not solved since it is a non-reacting gas. Its generation rate in the fuel channel, originating from the ammonia decomposition reaction, is handled by the ammonia mass balance using reaction stoichiometry based on eq (52).

To solve the coupled electrochemical, energy, and mass balance sub models, the individual residual equations are assembled into a single global residual vector of size (9N+5)x1. A corresponding state variable vector is defined, in which each entry represents an unknown variable at a given discretized location. The ordering of the variables in the state vector needs to be consistent with the residual vector, each residual equation having the appropriate state variable. Inconsistent indexing leads to the solver assigning unphysical values to the solved state variables.

In addition, an initial guess value vector is constructed, maintaining the indexing structure of the state vector. Note that Newton type solvers require more iterations and may fail to converge when the difference between the initial guess values and actual state variable solutions is large.

3) Results and Discussion

Following chapter provides model validation against published literature, three parametric studies as well as study conclusions and future implementations. Validation compares model ammonia decomposition kinetics with temperature dependent reaction rate - ammonia fractional conversion results provided by Barat et. al. [45]. Electrochemistry is validated against an j_{cell} -V_{cell} curve published by He et. al [50] for Pd doped ammonia fed PCFCs. Consistency checks regarding mass and energy conservation are conducted as well as numerical stability tests of species partial pressures approaching zero. Furthermore, three parametric studies examining the impact of increasing ammonia inlet flow rates, and average cell current density as well as PCFC temperature are presented. Lastly, the conclusion and future implementation sections provide an overview of methodology and findings, with discussion regarding further improvements and implications for system level analysis.

3.1) Validation and Model Consistency Evaluation

The validation methodology consists of experimental and model output comparisons, literature-based system behavior analysis as well as mass and energy conservation checks. Due to the absence of a single experimental dataset that directly replicates the modeled configuration (catalyst composition, cell geometry, and spatial resolution), the comparisons are intended to assess general physical consistency rather than enforce strict quantitative agreement.

The validation procedure is separated into three primary segments. First, ammonia decomposition kinetics are compared with the results published by Barat. This requires decoupling the ammonia decomposition submodel from the PCFC framework to remove the influence of spatially varying temperature and pressure fields arising from the coupled electrochemical system. Second, the electrochemical behavior of the model is evaluated through comparison with experimentally reported polarization curves for ammonia-fed PCFC systems. Although differences in catalyst materials and cell configuration prevent direct quantitative comparisons, the results provide a benchmark for assessing whether the model reproduces physically realistic voltage–current characteristics. Finally, a series of internal consistency checks are performed to verify the correctness of the numerical implementation. Mass and energy balance consistency checks are performed for each discretized point to verify whether each species balance has been implemented consistently. On the other hand, species gas channel and TPB pressures are confirmed to be within physically admissible bounds. Together, these checks ensure that the coupled multiphysics model adheres to fundamental conservation laws and produces stable, physically meaningful solutions. This layered validation framework enables a comprehensive assessment of the model despite the inherent limitations in direct experimental comparability, providing confidence in its predictive capability for analyzing ammonia-fed PCFC systems.

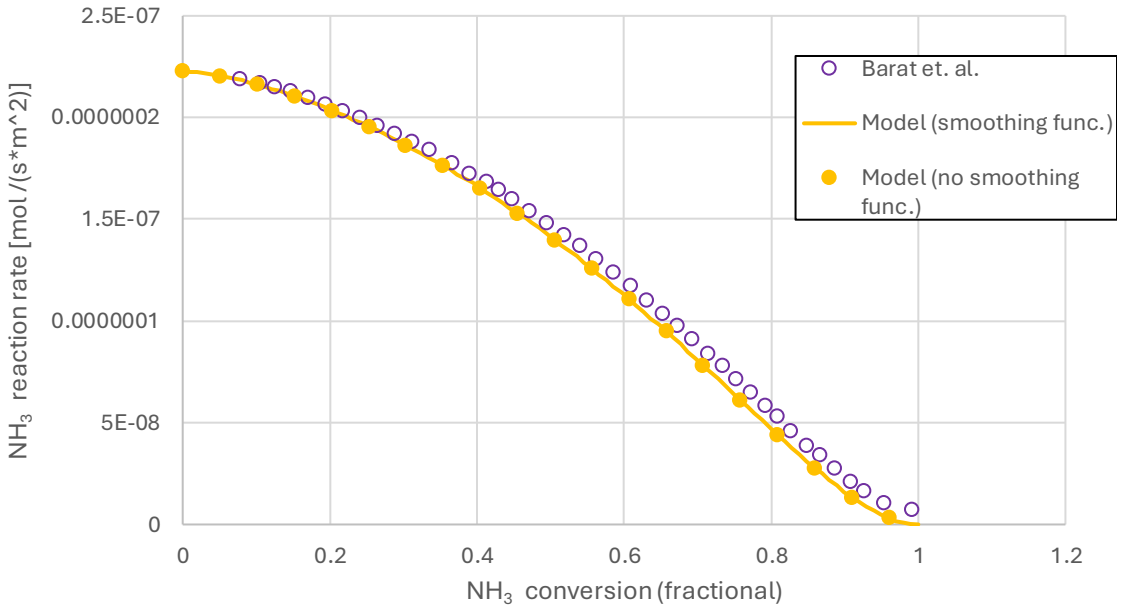

Figure 7 Comparison of model ammonia decomposition kinetics with Barat et. al. at 650 K

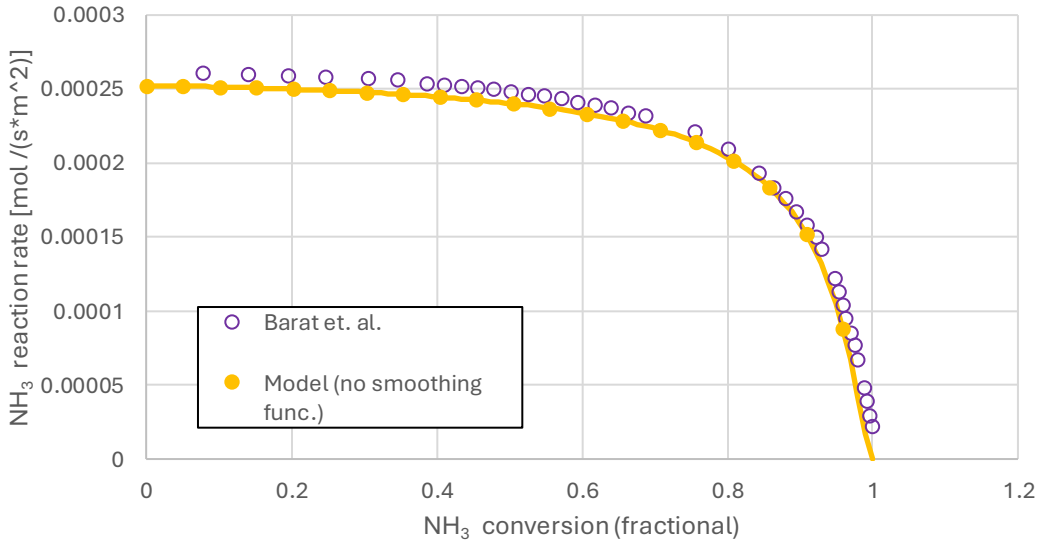

Figure 8 Comparison of model ammonia decomposition kinetics with Barat et. al. at 950 K

Figure 7 and Figure 8 describe the ammonia decomposition decrease with the drop in reactant availability**.** Decomposition kinetics are presented at a 650 K and 950 K case. Data is provided for outputs generated with implemented smoothing functions (yellow markers) as well as cases without smoothing (yellow line), ensuring the smoothing functions have

minimal impact on result physicality. Results are compared to the results provided by Barat et. al. [45] described by the purple markers.

At 950 K (Figure 7), the reaction rate remains relatively high and nearly constant over a wide range of low-to-moderate conversions, followed by a sharp decline as the conversion approaches zero. Initially the high temperature promotes high reaction rates with minimal hydrogen and nitrogen inhibition. However, at higher conversion factors, released hydrogen and nitrogen have a stronger inhibiting effect at catalyst sites, leading to a sharp drop in the reaction rate. consistent with the reversible nature of ammonia decomposition, where increasing product partial pressures drive the system closer to equilibrium. Thus, the sharp drop at the end represents the thermodynamic limit imposed by high conversion levels. In contrast, at 650 K (Figure 7), the reaction rate exhibits a more gradual and continuous decline across the entire conversion range.

At this lower temperature, the reaction kinetics are slower and are more sensitive to inhibition effects of hydrogen and nitrogen. Hence, the rate decreases slowly and without any major changes in reaction rate gradient. The matching smoothing and non-smoothing outputs indicate that the introduction of hyperbolic tangent and continuous max functions under specific parameters does not have an impact on ammonia decomposition kinetics. Comparing the model outputs to results provided by Barat et.al. [45] indicates that the models exhibit consistent ammonia decomposition curve shapes for both 650 K and 950 K cases. There is general agreement between the model predictions and reference data across all cases demonstrates that the Barat formulation has been correctly implemented, capturing both temperature-dependent kinetics and composition-dependent inhibition

effects. There is a small consistent offset which possibly indicates axis calibration issues during data digitization.

Electrochemistry:

The model outputs are compared to experimental polarization results provided by He et. al. The paper presents a Pd-doped proton-conducting perovskite oxide for direct ammonia-fueled PCFC operation at intermediate temperatures. The specific study is chosen as the direct ammonia fuel design reflects the modeling premise, enabling direct comparison of effects of ammonia on PCFC electrochemistry. The validation is quantified through voltage-current density curves, which are commonly provided by experimental papers. The current density – voltage behavior is investigated across 773 K, 823 K and 873 K, reflecting the operating conditions implemented in parametric studies in section 3.2)

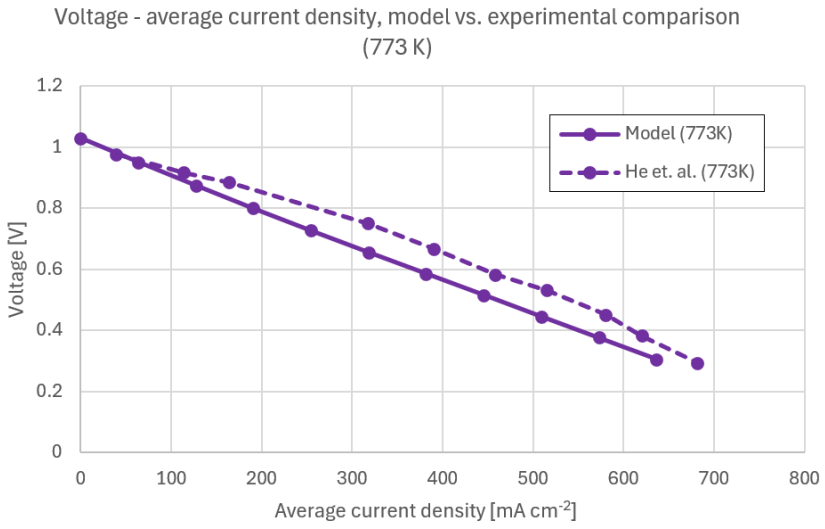

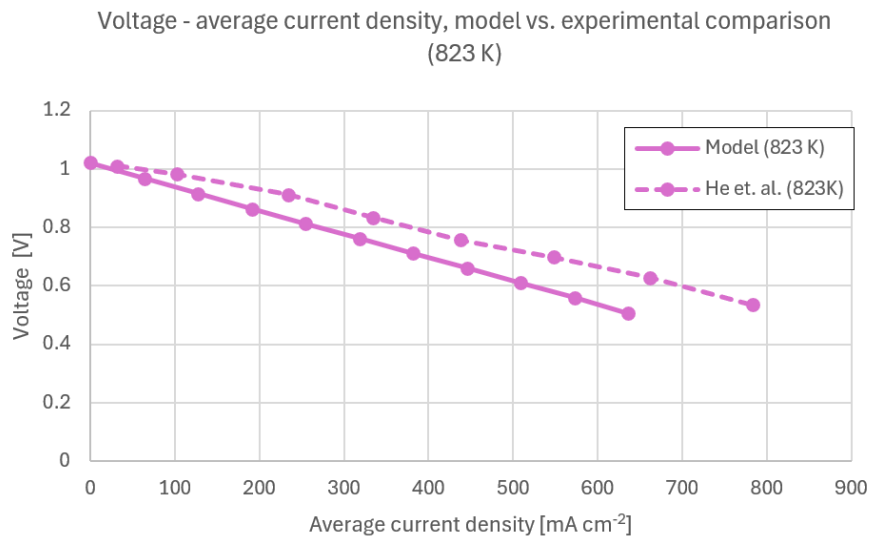

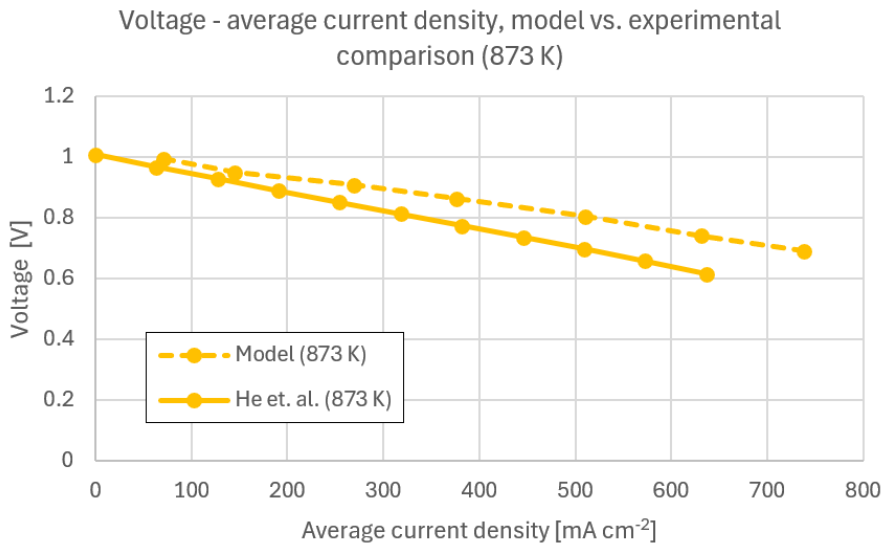

Table 7 Statistical analysis of model and He et. al. experimental results

Metric	773 K	823 K	873 K
R^2	0.9885	0.9966	0.9886
RMSE	0.0471	0.0653	0.1000
Max Err	0.0800	0.1438	0.1463
% Err	8.91%	12.88%	15.84%

Comparing the experimental and model results indicate consistent physics implementation inside the PCFC model, albeit with differences in behavior consistent across the temperature cases. Both datasets exhibit a decrease in voltage with increasing current densities, reflecting the cumulative influence of activation, ohmic, and concentration losses, while also demonstrating a similar temperature-dependent shift in performance. The datasets exhibit overall similar behavior, with R-squared values equaling 0. 988468, 0. 996607 and 0.988635 for 773 K, 823 K and 873 K cases respectively.

It seems that the implemented model consistently overestimates the PCFC overpotentials with the mean absolute error equaling 0.047096, 0.065342 and 0.099991, resulting in a lower voltage across each case relative to experimental data.

The behavior seems consistent across all temperature cases with similar overpotential values at lower current densities which start diverging with increasing cell current densities, with maximum errors reaching 0. 079964, 0.143765 and 0. 146323 V, and the model overpredicting overpotential losses by 8. 914143%, 12.88001% and 15.83595% on average.

At current densities approaching zero, the j_{cell}- V_{cell} curves from model and experimental outputs exhibit a strong overlap. This indicates that the Nernst potential equation is correctly implemented and yields accurate results.

A likely source contributing to experimental and model data discrepancy is an overestimated empirical cell ASR relationship. Systems where ohmic resistance is the highest overpotential source typically exhibit the linear j_{cell} - V_{cell} curve present in the current model. Note that different fuel cells may have widely ranging ASR values depending on

materials and preparation methodology. The ASR relationship used from [28] yield 0.839, 0.606 and 0.454 ohm $\cdot$ cm^2 at 773 K, 823 K and 873 K temperatures respectively. These values are physical but tend to be on the higher end for PCFCs, with papers reporting PCFC ASR values lower than 0.327 ohm $\cdot$ cm^2 at 873 K temperature [51]. At current model implementation, ohmic resistance overshadows the activation and concentration overpotential nonlinear behavior typically dominating at the higher or lower current density ranges. Thus, implementing a lower, more representative ASR relationship to the experimental fuel cell may decrease the model overestimation and match the shape of the j_{cell} - V_{cell} more accurately.

Note that error source may not be attributed to ASR only and other mechanisms may contribute to overall model electrochemical performance in different extents.

As the paper does not provide exact species inlet mass flows, it is uncertain whether reacting species experienced depletion under cell operating conditions. This raises a question regarding the extent of concentration losses during the experimental trials. This is further dependent on electrode preparation and diffusivity, as electrodes with optimized material properties typically result in improved species transport and lower concentration overpotentials. There is indication that species depletion is present in the experimental study for the 773 K case as evidenced from the slight voltage drops at current densities above approximately 600 mA $\cdot$ cm^{-2}. The model study was performed at species molar flow defined by equation 90 which are set to avoid species depletion. Depending on experimental setup, this could have led to model underestimating the concentration overpotential at higher current densities.

In addition, the model assumes symmetric charge transfer coefficients, which enabled expressing the Butler-Volmer equation in terms of a hyperbolic sine relationship. However, this assumption neglects individual electrode charge transfer kinetics, which are more complex on the cathode side. This can potentially reduce nonlinearity of the j_{cell} - V_{cell} curve at low and intermediate current densities.

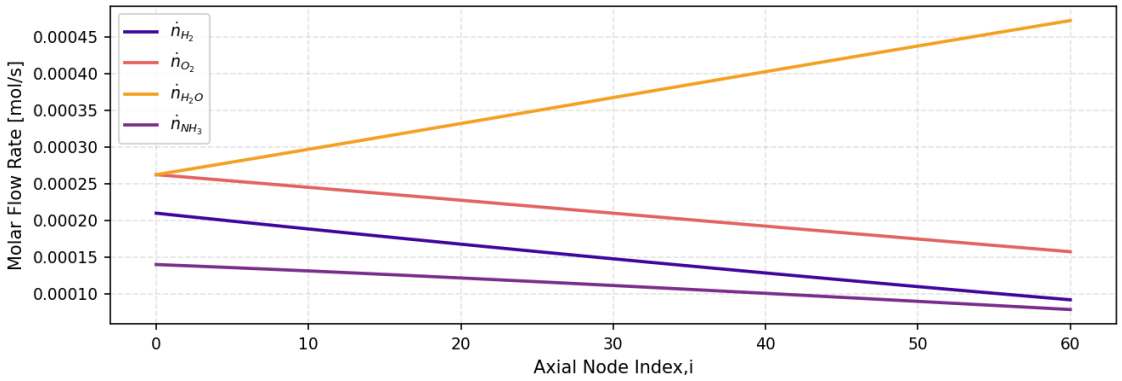

Figure 9 a) Species Molar Flow Profiles Consistency Check

Figure 9 represents a consistency check regarding species mass balance implementation. Species profiles are monotonic and physically bounded across the cell, indicating stable implementation of coupled species source terms and electrochemical consumption rates. Overall, it is supported by PCFC operating principles described in Section 1.3). Both hydrogen and oxygen experience a decreasing trend due to electrochemical consumption while water experiences a sharp increase through the water formation reaction at the cathode, described by equation (2) Note that based on equation (2) the gradient of H_2 decrease should match the gradient of H_2O, as both stoichiometric coefficients equal 1. However, this behavior is expected since hydrogen is produced by ammonia decomposition in parallel, confirming correct implementation of ammonia-hydrogen coupling.

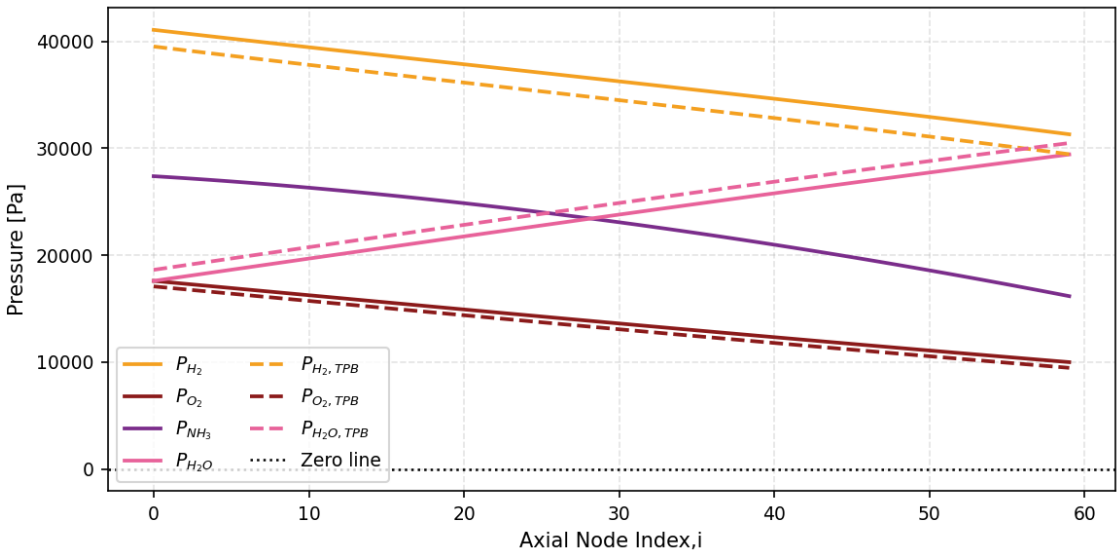

Figure 9 b) Species Partial Pressure Profiles Consistency Check

Note that the partial pressures of hydrogen and water are lower at the TPB than in the fuel channels. On the other hand, the partial pressure of water is higher at the TPB compared to the channels. This is physically consistent since hydrogen and oxygen are initially supplied at the channels and diffuse inside the electrodes to participate in electrochemical reactions. On the other hand, water is generated at the TPB and it diffuses through the cathode to enter the gas channel, corresponding to a higher pressure at the TPB.

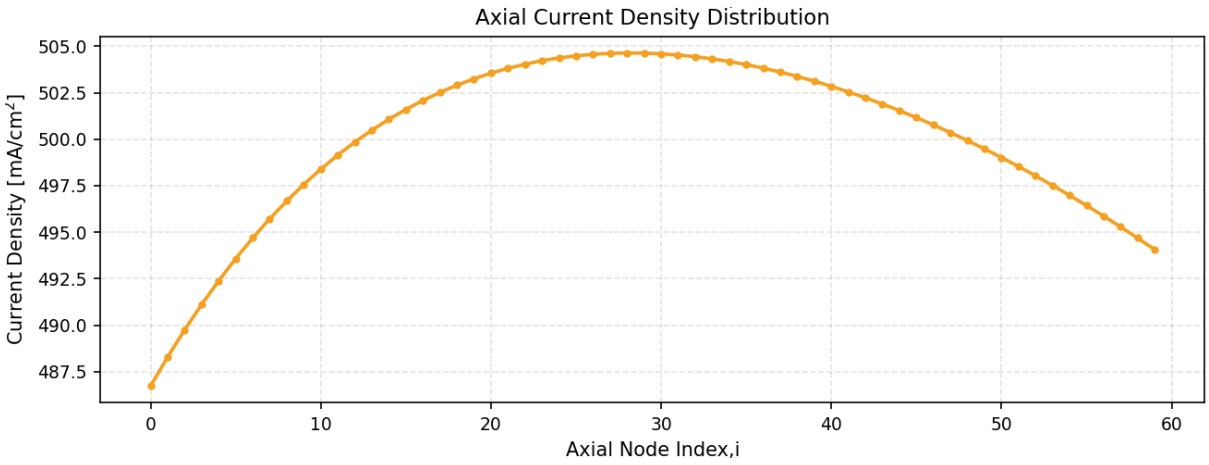

Figure 9 c) Axial Current Density Axial Profile Consistency Check

Figure 9 c) presents axially evolving cell current density. The plot is smooth, exhibiting lower current near inlet, an increasing trend towards the center and decline near outlet. This behavior captures competing thermal and concentration effects, evolving NH_3 decomposition, H_2 generation/consumption interplay as well as local Nernst potential variation.

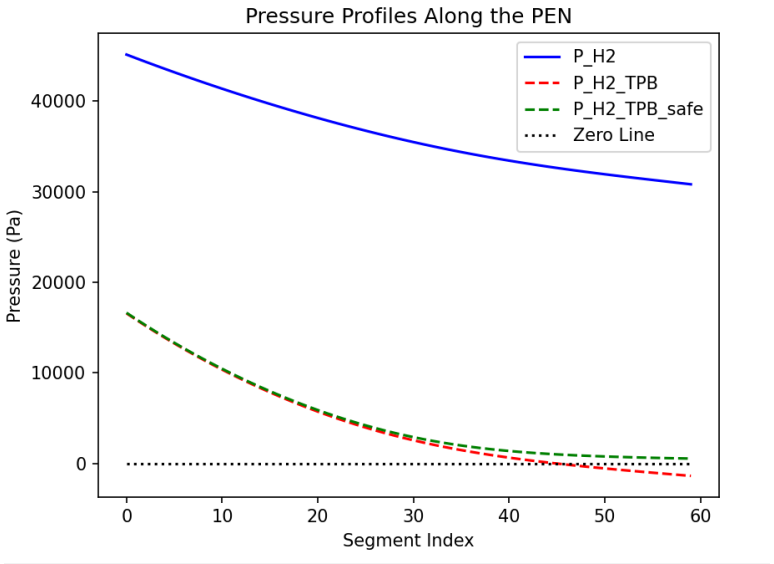

Figure 10 Hydrogen Partial Pressure Tanh and Continuous Max Smoothing Implementation Consistency Check

Figure 10 represents the implementation of numerical safety mechanisms such as tanh and continuous max smoothing, preventing partial pressures from reaching physically impossible values. The profile is tested at a high 1500 mA/cm^{-2} current density to increase the impact of transportation losses throughout the anode. The red dotted line represents the partial pressure without implemented smoothing mechanisms, reaching negative values at segment index $i \approx 45$. Green line indicates that the numerical safety mechanism has been correctly implemented as the partial pressure is kept at a positive range across the entire cell length.

Since the model is defined as steady state, the difference between the species inputs and outputs must equal zero, which must be verified for all the discretized points. This process is essential to ensure that species consumption and generation terms are implemented correctly. Each species is individually evaluated in addition to the total mass balance.

Overall, the balances tend to be non-zero numbers. However, this is caused by numerical solvers architecture where convergence occurs when a set of values satisfies the residual function withing a certain degree of tolerance. The maximum value calculated from the mass conservation validation is $1.64 \cdot 10^{-15}$ which is negligible relative to the magnitude of the respective molar mass flow.

3.2) Parametric Analysis of Model Performance

3.2.1) Ammonia Molar Flow Parametric Study

Application of ammonia in PCFCs requires analysis of the inlet fuel makeup on PCFC operation. Following parametric study investigates the impact of increasing ammonia inlet molar flows on species molar profiles, electrochemical performance, PEN temperature profiles, ammonia utilization as well as power density outputs. The rationale is to determine ammonia inlet molar flows which balance electrochemical performance, hydrogen supply and ammonia utilization. This insight helps determine how amounts of delivered ammonia inform cell operation and considerations for system level designs. The study represents five ammonia inlet molar flow rate cases ranging from 0.16 mmol/s to 0.34 mmol/s, totaling five trials.

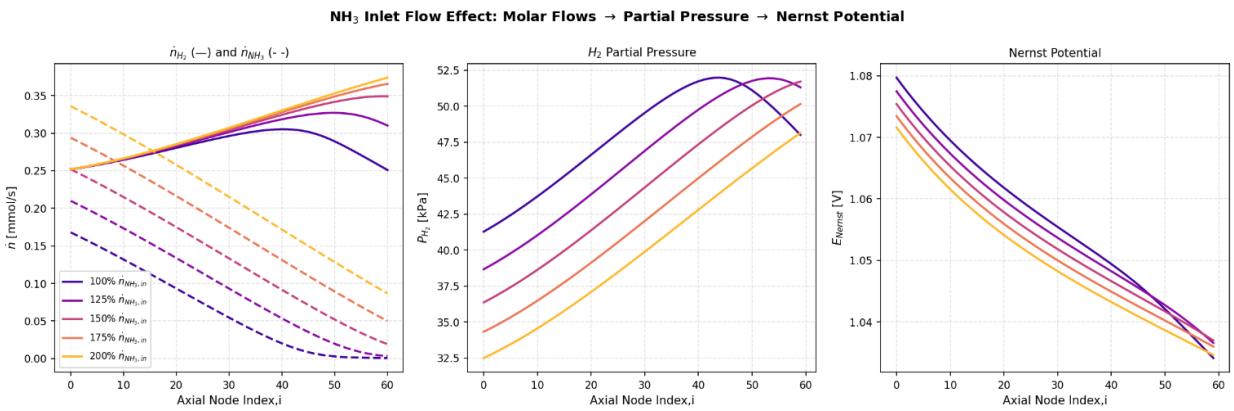

Figure 11 Effect of Ammonia Inlet Composition on Axial NH_3/H_2 Molar Flows, H_2 Partial Pressure, and Nernst Potential

Figure 11 represents coupled behavior of axially evolving NH_3 & H_2 flow rates, H_2 partial pressure and Nernst potential under five NH_3 inlet flow rates.

Inlet H_2 molar flow rate is kept constant at 0.25 mmol/s for each case. At the inlet, the 100% NH_3 case is related to the highest inlet partial pressure as it has the highest molar fraction at gas channel partial pressure constant across every case. This is further reflected in improved electrochemical performance as higher channel pressures increase the Nernst potential as seen on the right plot. Increasing inlet NH_3 compositions decreases the Nernst potential, resulting in an approximate 0.09 V decrease between the 100% and 200% NH_3 cases. Under the operating conditions of the model, NH_3 thermo-catalytic decomposition is higher than the electrochemical consumption of H_2, leading to an initial increase in hydrogen molar flow rates. This is also reflected in the increase in partial pressure of H_2 across the cell length. Interestingly, the increase in hydrogen partial pressure does not result in an increase in Nernst potential. This can be interpreted through the oxygen reduction reaction at the cathode causing shifts in oxygen and water partial pressures.

At approximately node index 40, ammonia is depleted for the lowest ammonia inlet scenario. Hydrogen experiences electrochemical consumption only and the molar flow rate starts decreasing accordingly. As hydrogen partial pressure drops, Nernst potential experiences a higher rate of decrease, becoming the lowest out of every other case.

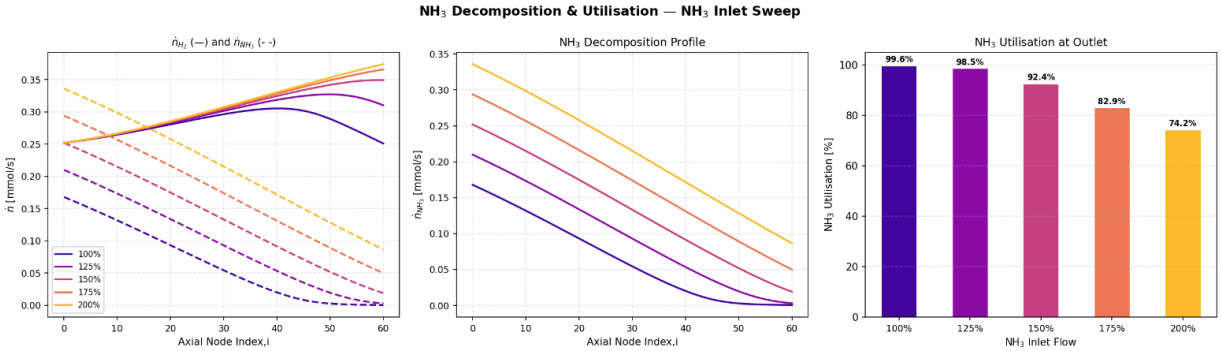

Figure 12 Effect of Ammonia Inlet Composition on NH_3 Decomposition Profiles and Fuel Utilization

This figure provides information on utilization of ammonia during PCFC operation under increasing inlet flow rates. Left plot represents the molar profiles of ammonia described with the dashed line. Middle plot isolates the NH_3 profile, while the overall utilization factors are represented on the right plot. This helps inform choice of operating conditions, system design and any required NH_3 recycling strategies in cases where unreacted ammonia would remain at the system outlet.

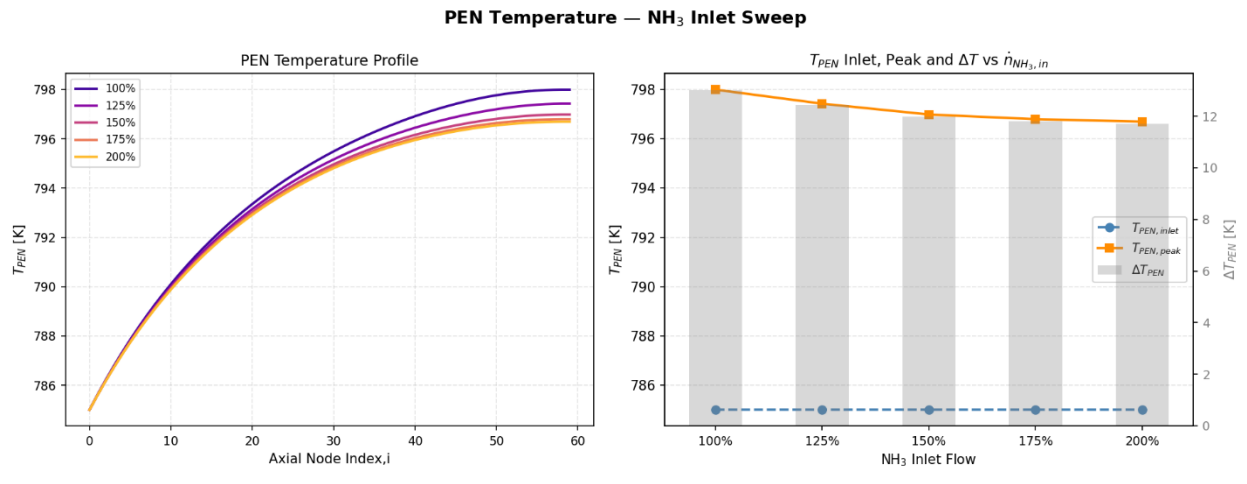

Figure 13 Effect of Ammonia Inlet Composition on PEN Temperature Distribution and Thermal Rise

Figure 13 represents the axial temperature profile of the PEN (left), along with the corresponding inlet and peak temperature variations for different ammonia inlet molar flow rates (right). The PEN is specifically examined because the model assumes that ammonia decomposition directly influences only the PEN energy balance.

Initially, the PEN temperature exhibits similar behavior across all cases, showing a consistent increase along the axial direction. Although ammonia decomposition is endothermic, its cooling effect is smaller than the combined heat input from electrochemical reactions. Therefore, the PEN temperature still increases axially.

Differences between cases become more apparent in the downstream region. The 100% and 125% ammonia inlet cases exhibit a slightly steeper temperature rise compared to higher inlet flow rates. This behavior can be attributed to earlier depletion of ammonia, which reduces the magnitude of the endothermic decomposition sink. Consequently, the

energy balance becomes increasingly dominated by electrochemical heat generation, particularly from the oxygen reduction reaction.

This effect is reflected in the peak temperature comparison, where an approximate 1.8 K difference is observed between the 100% and 200% cases. The relatively small difference between the cases indicates that while ammonia decomposition has an impact on PCFC thermal profiles, it does not dominate them.

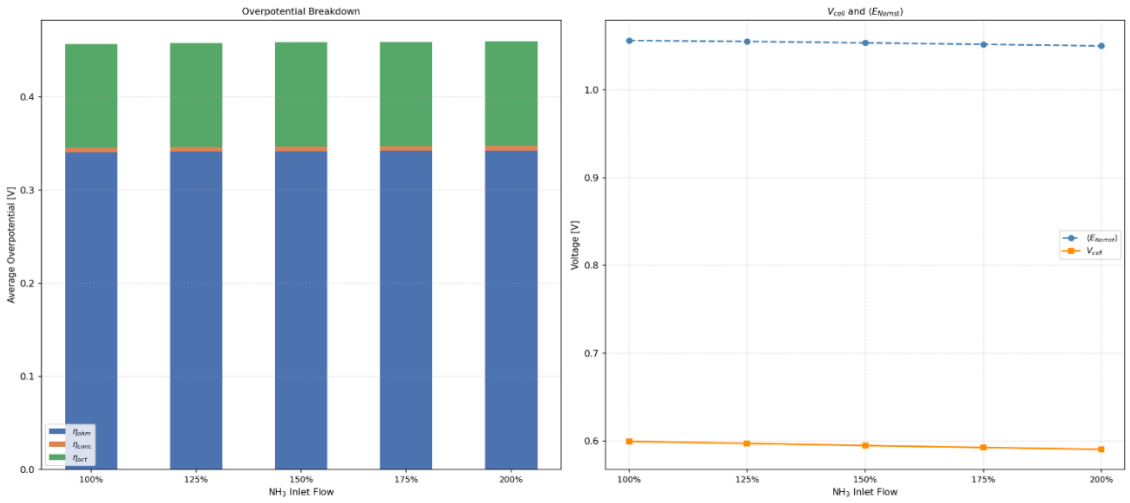

Figure 14 Effect of Ammonia Inlet Composition on Overpotential Contributions and Cell Voltage in PCFC

Figure 14 describes the total electrochemical losses divided into axially averaged ohmic, concentration and activation overpotentials (described in blue, orange and green respectively). The middle figure maps the losses into averaged Nernst and cell operating voltages described with light blue and orange respectively.

The electrochemical performance indicates that variations in NH_3 inlet flow have a relatively minor impact on the overall overpotential distribution. The axially averaged ohmic,

activation, and concentration overpotentials remain nearly unchanged across the investigated range, suggesting that electrochemical losses are not directly sensitive to ammonia concentration under the present operating conditions.

The observed performance trends are primarily governed by changes in gas-phase composition rather than direct ammonia-induced catalyst inhibition. The present model does not include surface reaction kinetics or competitive adsorption effects associated with ammonia interaction at the catalyst. Instead, concentration overpotentials are formulated based on the transport and availability of electrochemically active species (H_2, O_2, and H_2O) between bulk channel conditions and the triple-phase boundary (TPB). Within this framework, ammonia does not directly participate in the electrochemical reaction and therefore does not explicitly contribute to TPB kinetics. However, the model can indirectly capture impact of ammonia through influence on local species partial pressures. Increased ammonia content reduces the hydrogen partial pressure baseline from which TPB partial pressures are calculated, affecting both the Nernst potential and associated concentration losses.

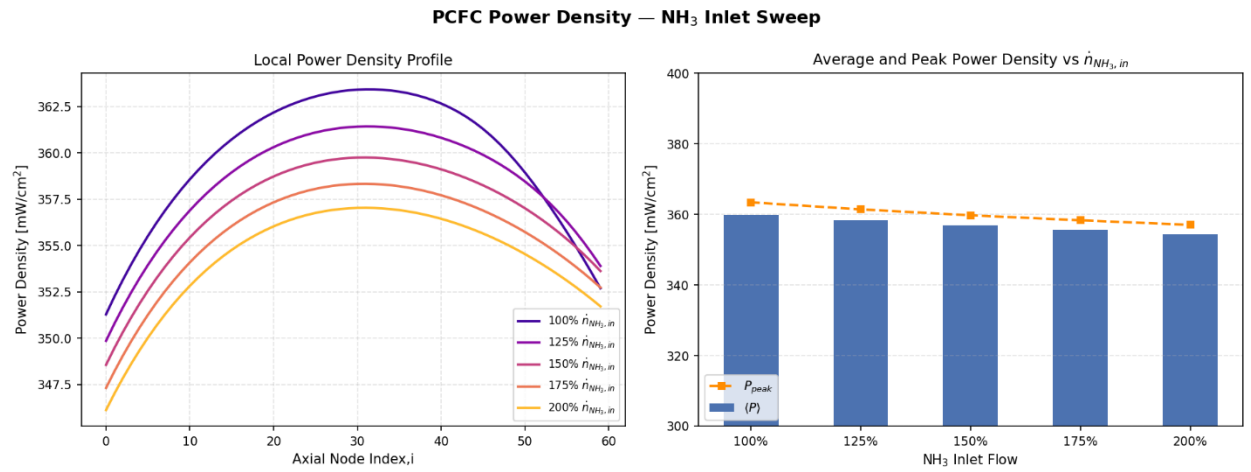

Figure 15 Effect of Ammonia Inlet Composition on Local, Average, and Peak Power Density in PCFC

The PCFC power density profiles indicate improved power delivery at lower ammonia inlet flow rates.

3.2.2) Current Density Parametric Study

Following parametric study investigates the impact of increasing current density on molar profiles, electrochemical performance, PEN and interconnect temperature profiles, ammonia decomposition as well as power density outputs. The rationale is to determine average cell current density operations which balance overpotential losses and cell current density, delivering highest power density. This is a critical insight which determines cell operation and design considerations for system level designs.

Note that the model may not support conditions where reactants are fully depleted as described in section 2.8). Thus, a parametric study with fixed inlet molar flow rates may result in divergence especially at a larger current density range. Hence, the paper does not isolate the effects of increasing current density, instead implementing a proportional increase in molar flow rate inputs with increasing electrochemical load. The molar inlet flow rates are defined as:

$$\dot{n}_{H_2,\text{in}} = \frac{j_{\text{cell,avg}} A_{\text{active,total}}}{2F} C_{H_2}, \dot{n}_{NH_3,\text{in}} = \frac{j_{\text{cell,avg}} A_{\text{active,total}}}{3F} C_{NH_3}, \quad (90)$$

$$\dot{n}_{O_2,\text{in}} = \frac{j_{\text{cell,avg}} A_{\text{active,total}}}{2F} C_{O_2}$$

where C_{H_2}, C_{NH_3}, and C_{O_2} are scaling factors based on the defined species ratios at the inlet.

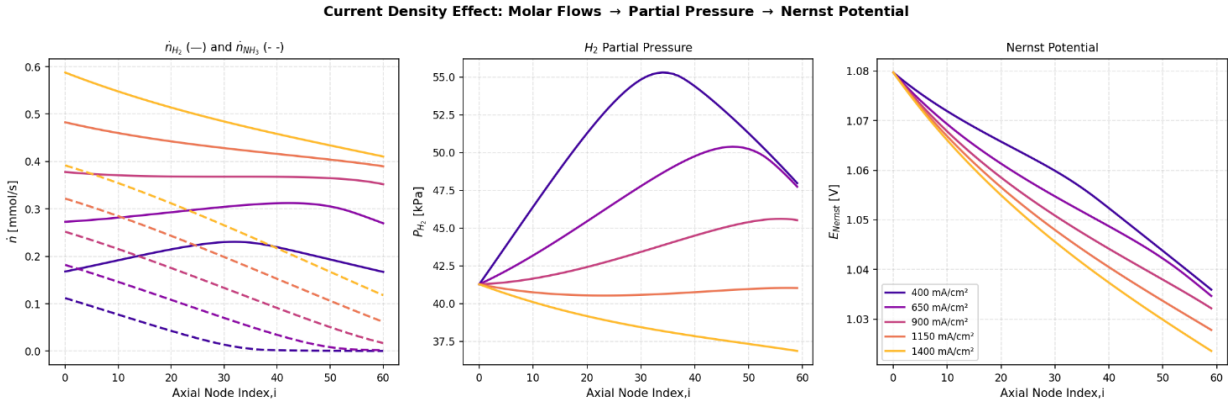

Figure 16 Effect of Current Density on Axial NH_3/H_2 Molar Flows, H_2 Partial Pressure, and Nernst Potential

This figure illustrates the coupled effect of increasing current density on axial species transport, thermodynamic state, and electrochemical potential within the PCFC.

As current density increases, NH_3 consumption is accelerated along the cell, leading to a more rapid decline in NH_3 molar flow and a corresponding increase in H_2 production near the inlet. However, at higher current densities, H_2 is also consumed more aggressively by the electrochemical reaction, resulting in an overall reduction in H_2 molar flow toward the outlet compared to lower current cases.

This interconnected mechanisms directly influence the H_2 partial pressure profile. At lower current densities, H_2 accumulates along the channel, producing a peak in partial pressure.

In contrast, higher current densities suppress this buildup due to increased electrochemical consumption, leading to flatter or even decreasing partial pressure profiles.

Consequently, the Nernst potential decreases more sharply with increasing current density. The reduction in H_2 partial pressure, combined with ongoing fuel consumption along the cell, lowers the local electrochemical potential, resulting in a steeper axial voltage drop at higher loads.

Overall, the figure highlights the transition from a fuel-rich regime at low current density to a fuel-limited regime at high current density, demonstrating the strong coupling between reaction kinetics, mass transport, and electrochemical performance.

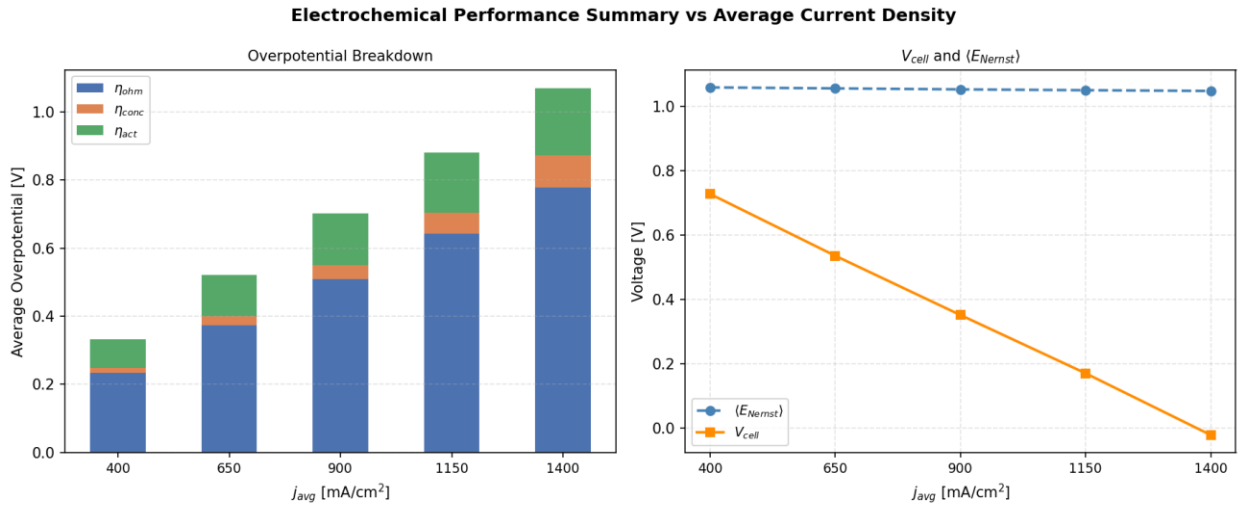

Figure 17 Effect of Current Density on Overpotential Contributions and Cell Voltage in PCFC

Increased cell current density is associated with an increase in each overpotential type. Higher cell current densities increase the pressure gradient between the species channel and TPB pressures, which when approaching 0 kPa increases the concentration

overpotential. On the other hand, higher current densities increase the activation overpotential as faster electrochemical reaction rates require a larger driving force to overcome charge-transfer kinetics at the electrodes. The Butler-Volmer kinetics governing charge transfer at the anode and cathode require an exponentially increasing overpotential to sustain higher reaction rates. Ohmic losses scale linearly with current density through the area-specific resistance (ASR) of the electrolyte and interconnect. As seen in Figure 15, η_{ohm} is the dominant loss mechanism across all operating points, reflecting the high ASR characteristic of lower-temperature PCFC operation. Thus, as electrical current is supplied by the cell is increased, the increasing overpotentials reduce the operating voltage, resulting in decreased delivered power, further described in Figure 21. Note that the model converges even for case where the required voltage is higher than the Nernst potential. This supports the statement in section 2.1). that the defined cell current density enforces operating conditions instead of being defined by them.

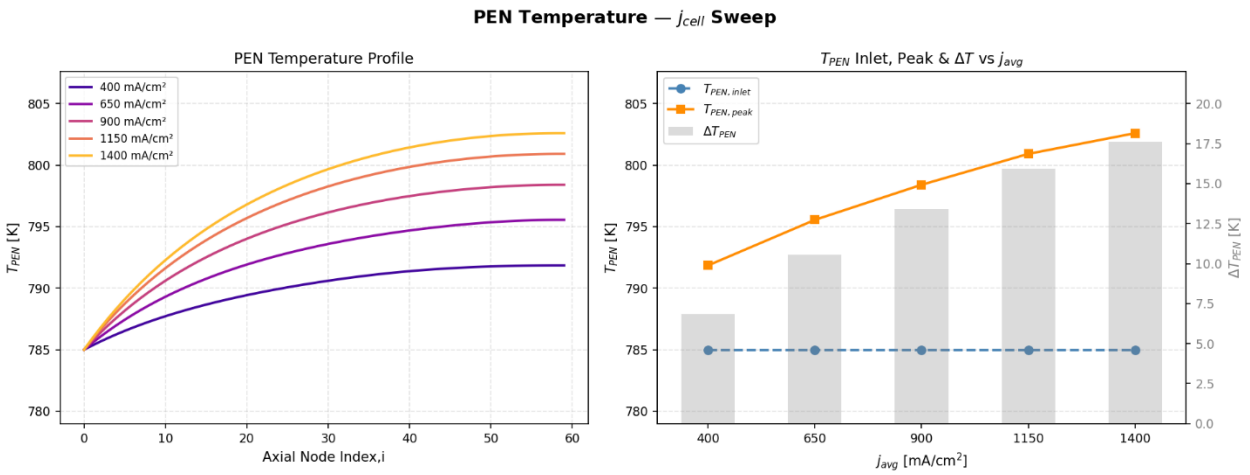

Figure 18 Effect of Current Density on PEN Temperature Distribution and Thermal Rise

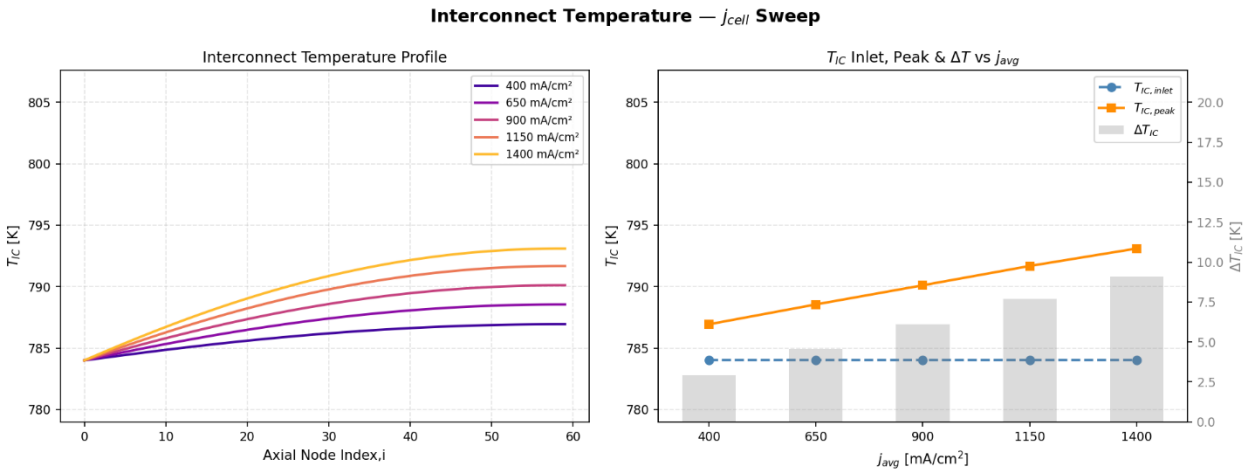

Figure 19 Effect of Current Density on Interconnect Temperature Distribution and Thermal Gradients

The cell current density sweep study includes both PEN and interconnect temperatures since the model implements current density dependent terms such as ohmic heating in interconnect energy balance and electrochemical reactions in the PEN energy balance.

Temperature rise is monotonic for both interconnect and PEN profiles. PEN experiences a higher rise at approsimately 17.5K compared to 9.5 K rise at the interconnect. This indicates that electrochemical reactions generate more heat compared to interconnect ohmic resistance. Interestingly, moderate outlet differences between the PEN and interconnect indicate somewhat weaker conductive heat transfer between the elements.

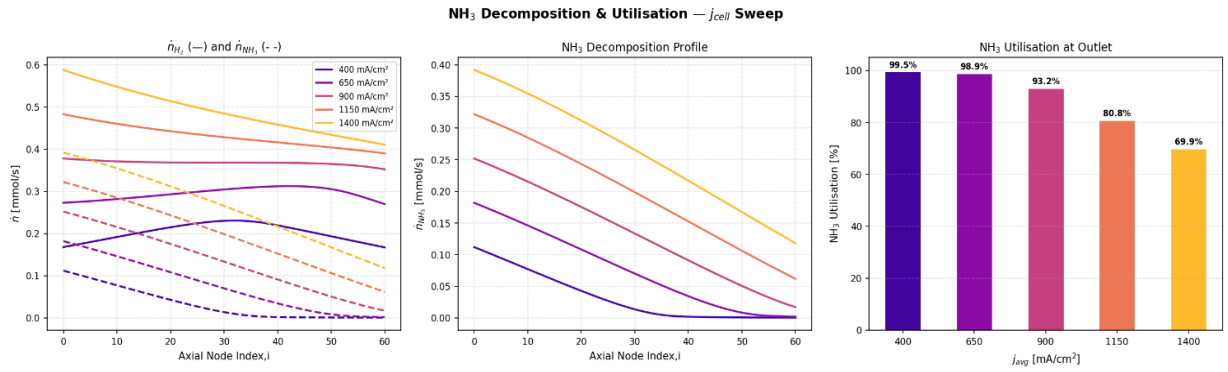

Figure 20 Effect of Current Density on NH_3 Decomposition Profiles and Fuel Utilization

Figure 20 describes the utilization of ammonia under increasing current density regimes. The results indicate that increasing current density increases hydrogen consumption and reduces ammonia conversion along the cell, leading to progressively lower NH_3 utilization at the outlet. While lower current densities achieve near-complete decomposition, higher current densities shift the system toward a fuel-limited regime, with significant unreacted ammonia remaining. Overall, these insights guide the choices in NH_3 flow rates as well as current densities required for balanced reactant supply and consumption during system operation.

Figure 21 Effect of Current Density on Local, Average, and Peak Power Density in PCFC

Figure 21 provides essential information guiding the choice of operating conditions of the fuel cell. It illustrates the effect of increasing current density on both the spatial distribution and overall magnitude of power density in the PCFC.

The local power density profiles (left) show that current densities in range of (400–900 mA/cm^2) maintain relatively high and uniform power output along the channel. The 650

mA/cm^2 case achieves the highest local power density, indicating an optimal operating point where kinetic losses and fuel utilization are favorably balanced.

Performance begins to deteriorate at current densities (<mA/cm^2) with power density dropping by 130 (mW/cm^2) between the 900 mA/cm^2 and 1150 mA/cm^2At the highest current density (1400 mA/cm^2), the power density becomes negative across the entire cell, indicating that the cell voltage has dropped below zero and the system is no longer operating in a power-generating regime. In this case, both the peak power density and average power density are negative.

Overall, the figure highlights the existence of an optimal current density for maximum power output and demonstrates the transition from efficient operation to loss-dominated behavior at high loads.

3.2.3) PCFC Inlet Temperature Parametric Study

The following parametric study investigates the impact of increasing inlet temperature on molar profiles, electrochemical performance, PEN temperature distributions, ammonia decomposition, and resulting power density outputs. The rationale is to evaluate how temperature-dependent kinetics and transport properties influence cell performance, particularly through enhanced reaction rates, reduced activation losses, and improved fuel utilization. The results from the analysis can inform decisions on heat integration strategies, operating limits as well as required ammonia inputs.

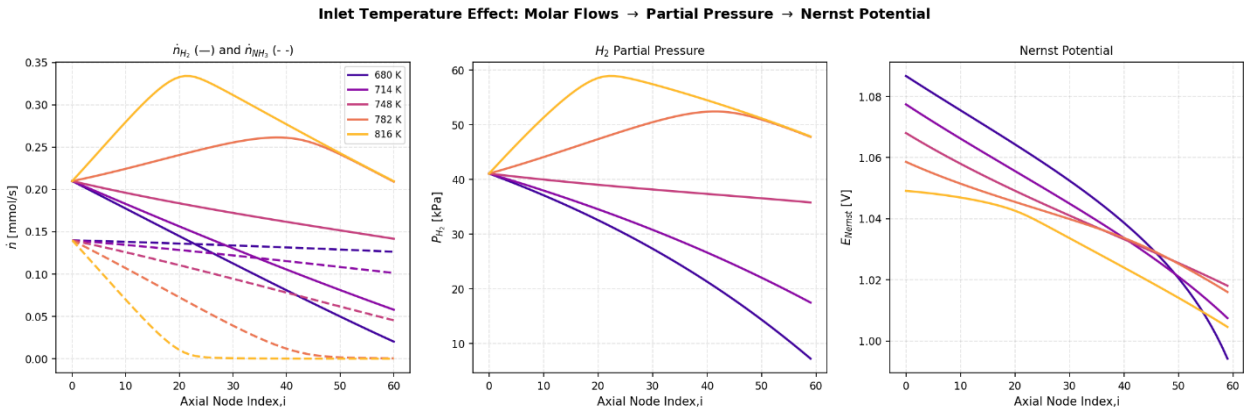

Figure 22 Effect of Temperature on Axial NH_3/H_2 Molar Flows, H_2 Partial Pressure, and Nernst Potential

Figure 22 describes the influence of inlet temperature on species transport, corresponding hydrogen partial pressure, and the resulting Nernst potential along the channel. Ammonia (dashed lines) and hydrogen (solid lines) inlet flow rates are both fixed at 0.14 and 0.21 mmol/s respectively. A clear decomposition pattern can be noticed under increasing temperature values. The left plot presents the axial molar flow rates of H_2 and NH_3 for each inlet temperature. Increasing inlet temperature leads to more rapid NH_3 decomposition, as indicated by the steeper decline in NH_3 molar flow and earlier depletion along the channel. This results in increased H_2 production, with higher temperature cases exhibiting a pronounced rise in H_2 molar flow near the inlet followed by gradual consumption downstream due to electrochemical reaction.

The middle plot shows the corresponding H_2 partial pressure profiles. The increased rate of NH_3 decomposition at higher temperatures elevates the local H_2 partial pressure, particularly in the upstream region. However, as H_2 is consumed along the channel, the partial pressure decreases toward the outlet. Lower temperature cases show reduced H_2 generation and therefore lower overall H_2 partial pressures throughout the domain.

The right plot maps the impact of composition changes into the Nernst potential. Higher inlet temperatures generally result in lower initial Nernst potentials due to the temperature dependence of the equilibrium term, but this effect is partially offset by increased H_2 availability. As the flow progresses downstream, the Nernst potential decreases across all cases, with the rate of decline influenced by the balance between hydrogen consumption and production. Higher temperature cases tend to maintain more stable Nernst potentials over a larger portion of the channel due to enhanced upstream hydrogen generation, although convergence between cases is observed near the outlet where depletion effects become dominant.

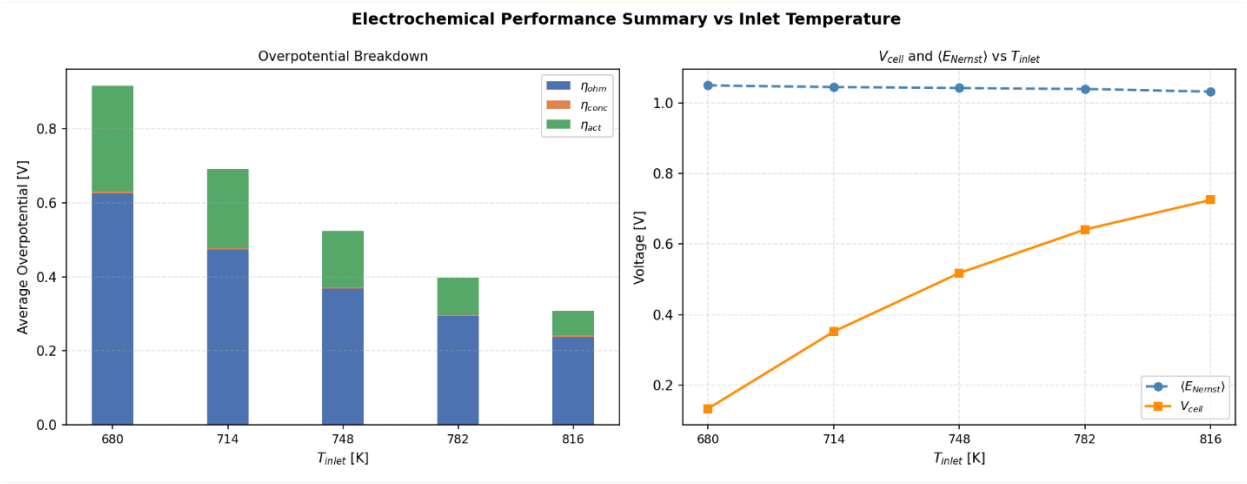

Figure 23 Effect of Temperature on Overpotential Contributions and Cell Voltage in PCFC

Figure 23 summarizes the impact of inlet temperature on the electrochemical performance of the system, including the distribution of overpotential losses and the corresponding cell and Nernst voltages. The left plot represents the axially averaged overpotential breakdowns expressed through ohmic (blue), concentration (orange) and activation (green) overpotentials. Increasing inlet temperature results in a consistent decrease in each overpotential component. Ohmic resistance experiences a decrease as increasing cell

temperature decreases the area specific resistance described in equation (16). Nevertheless, ohmic overpotential remains the largest overpotential contributor across the entire temperature range. Elevated temperatures are correlated with improved electrochemical reaction kinetics, which are reflected with decreased activation losses. On the other hand, concentration losses are limited across the temperature range and exhibit negligible changes across the temperature range. This is primarily a result of defined species inlet flow rates, which remain sufficiently high to maintain positive species TPB partial pressures. The overall reduction in total overpotential indicates improved electrochemical performance at higher inlet temperatures. The right plot maps these reductions into the corresponding cell operating voltage and averaged Nernst potential. The Nernst potential remains relatively constant across the temperature range, with only a slight decrease observed at higher temperatures due to thermodynamic effects. Note that this happens because Nernst potentials at lower temperature simulations are initially highest and subsequently experience the highest relative drop. Axially averaging this behavior results in a similar, yet slightly lower average Nernst potential for increased temperatures.

In contrast, the cell voltage increases significantly with inlet temperature, reflecting the reduction in irreversible losses observed in the overpotential breakdown.

The decreasing difference between Nernst potential and cell voltage indicates that higher temperatures enable operation closer to the thermodynamic limit of the PCFC.

Overall, the results indicate that increasing inlet temperature enhances performance primarily through reductions in ohmic and activation overpotentials, while average PCFC maximum operating potential remains negligibly different.

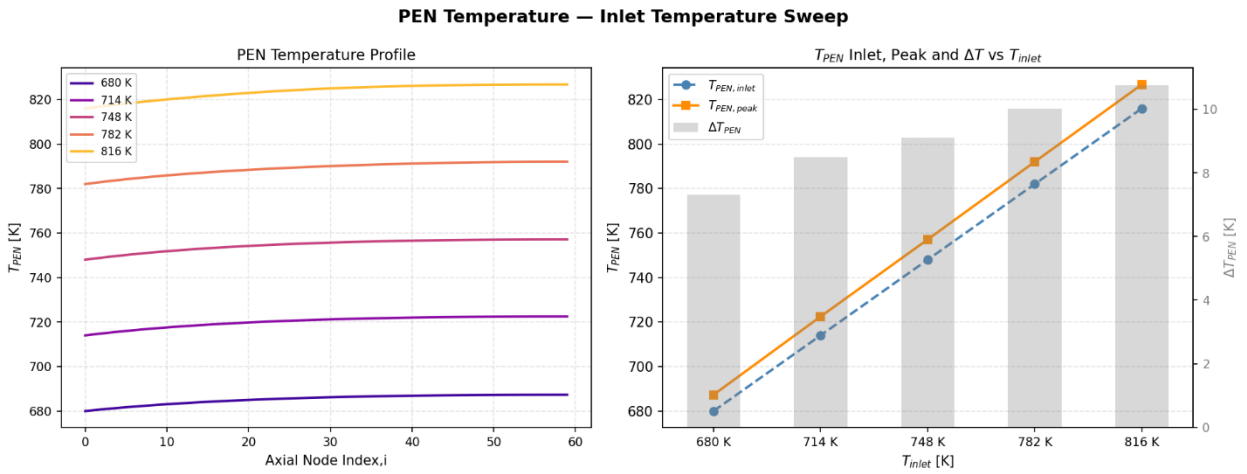

Figure 24 Effect of Inlet Temperature on PEN Temperature Distribution and Thermal Rise

The left figure confirms that each inlet temperature results in an overall increase across the cell. However, the right figure indicates that the increasing inlet temperature results in a larger change in temperature between the inlet and peak outlet. Between the 680 K and 816 K cases, this results in a difference of approximately 4 K. This can be interpreted as an impact of coupled electrochemical and thermal processes. Higher inlet temperatures increase reaction rates, leading to increased hydrogen production and higher current densities. Higher current densities in turn increase the ORR reduction rate which is a strongly exothermic reaction, resulting in an increased difference between inlet and outlet temperatures.

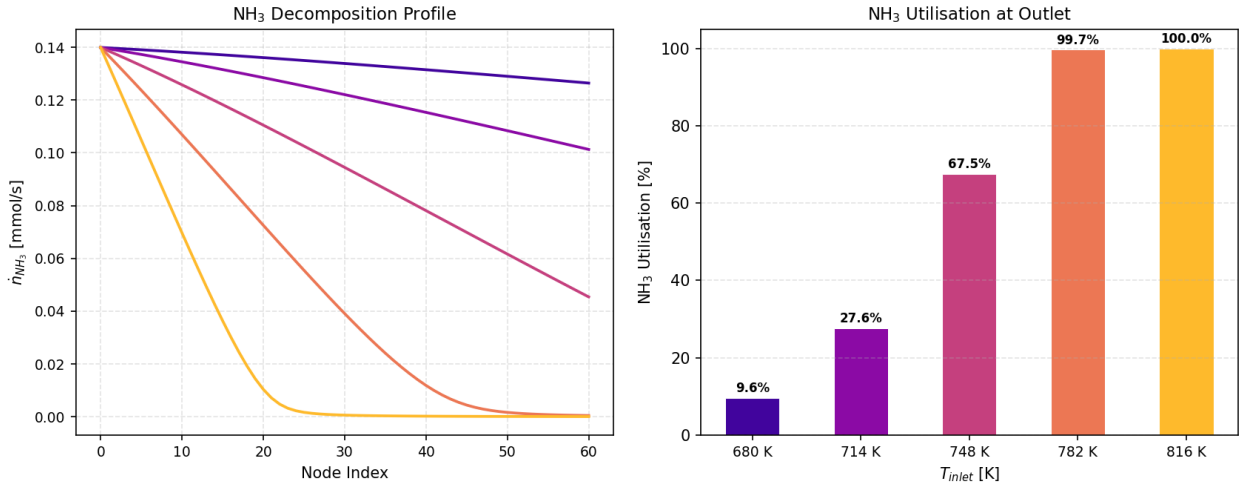

Figure 25 Effect of Temperature on NH_3 Decomposition Profiles and Fuel Utilization

Figure 25 illustrates the effect of inlet temperature on ammonia decomposition and overall utilization across the PCFC. Expectedly, higher temperatures have a strong impact on the overall utilization of ammonia across the cell. At 680 K the reaction seems sluggish as only 9.6 % of ammonia is utilized in the PCFC. On the other hand, cases above 782 K indicate effectively full ammonia decomposition. Note that the 782 K case has 99.7 % ammonia utilization which is mostly a result of numerical properties of the model as ammonia approaches the $n_{NH3} > 0$ asymptote. The overall behavior indicates that the system is kinetically limited at low temperatures, where insufficient thermal energy leads to slow NH_3 decomposition. These operations would require either changing the inlet ammonia feed or implementing anodes with higher levels of catalysts to improve yield. These results are further useful for future system level design framework as they determine the necessity of recycling units at the outlet which ensure higher ammonia decomposition and hydrogen utilization.

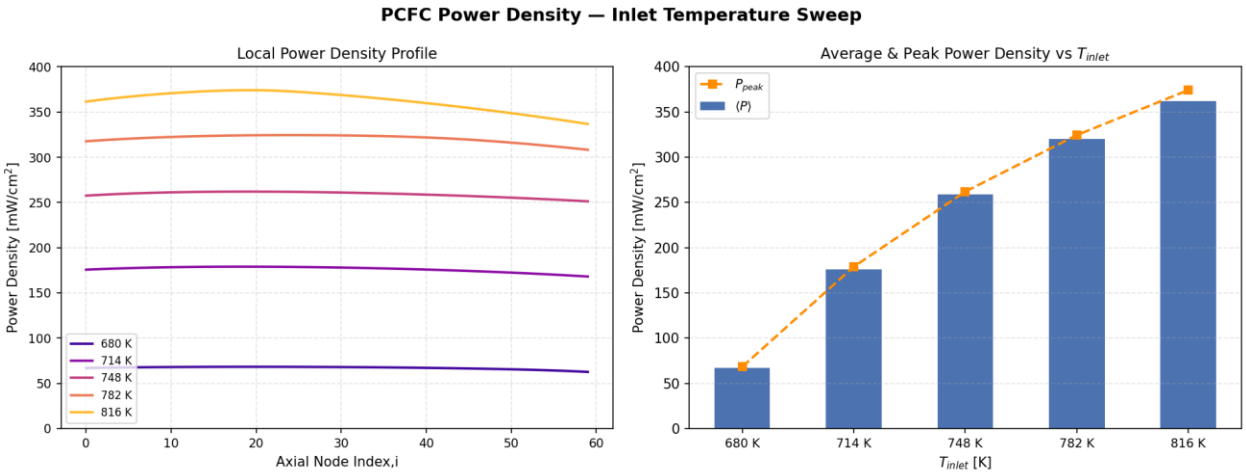

Figure 26 Effect of Temperature on Local, Average, and Peak Power Density in PCFC

The decrease in overpotentials with increasing cell operating temperature results in improved power density outputs. At temperatures such as 680 K, power density remains low with a minimal difference between the average and peak power densities delivered, as ammonia decomposition and subsequent hydrogen electrochemical consumption remain limited. However, the (680K – 748K) range experiences the strongest increase in cell power density outputs. At 782 K and 816 K temperatures the change in power density becomes less pronounced, as the overpotentials become less temperature dependent at upper temperature ranges. In addition this suggests that once NH_3 utilization approaches completion, further gains are increasingly limited by electrochemical or transport losses compared to fuel availability alone. Note that while operation at the elevated temperatures delivers the highest power density, these operating ranges introduce additional limitations such as higher materials degradation, higher energy inputs and lower PCFC lifespan, meaning that optimal operation needs to balance between these factors.

3.3) Conclusions

The developed PCFC model represents a novel reduced-order, one-dimensional framework that integrates ammonia decomposition kinetics with electrochemical, energy, and mass balance formulations. The model captures the coupled interaction between chemical reactions, species transport, and electrochemical performance, providing computationally efficient simulation of ammonia-fed PCFC systems.

The ammonia inlet molar flow rate, average current density and temperature parametric studies indicate several characteristic behaviors:

- H_2 partial pressure rises with higher inlet flow, maintaining a higher Nernst potential. Lower ammonia inlet flow rates result in depletion downstream causing sharper drops in Nernst potential, while higher inlet molar flow rates exhibit more consistent behavior across the PCFC.
- PEN temperature rise is moderate, higher flow rates slightly moderate thermal gradients due to enhanced endothermic NH_3 decomposition absorbing heat. Thus lower 0.16 mmol/s NH_3 flowrate results in a ~13 K temperature increases while 0.34 mmol/s NH_3 flowrate results in an ~11.5 K increase across the cell.
- Higher current density increases electrochemical H_2 consumption via Faraday's law. Under lower cell current densities NH_3 decomposition is stronger than electrochemical consumption of H_2 leading to initial increase in H_2 molar flow and partial pressure. Higher cell current densities consume H_2 faster than H_2 is released through NH_3 decomposition, leading to sustained decrease in H_2 molar flow and partial pressure.

- PEN temperature rises markedly with current density due to ORR heat generation and ohmic dissipation. Interconnect temperature follows, reflecting Joule heating. Larger axial gradients observed at high load.
- Average overpotential losses increase by ~450 % between 4000 A m^{-2} and 14000 A m^{-2}. Ohmic losses dominate across the average cell current density range, with an increase in each overpotential loss type with increasing cell current density.
- Under defined operating conditions of the PCFC, 6500 A m^{-2} current density results in the highest cell power density output. The cell experiences a sharp decrease in power output under current densities above 9000 A m^{-2}, representing less sustainable operation.
- Higher temperatures increase the decomposition rate of NH3, leading to an increasing H2 partial pressure. Upon depletion, hydrogen experiences a decrease as it only is electrochemically consumed
- Nernst potential varies with temperature through both ΔG_{ORR} and partial pressure changes. Increased H_2 availability at high temperature partially offsets the thermodynamic Nernst reduction.
- Activation overpotential decreases with temperature (Arrhenius kinetics). Ohmic losses also decrease as ASR is temperature dependent. Overall, increasing temperature promotes electrochemical performance of the cell, with ~65% overpotential decrease between 680K and 816K cases.
- Decomposition is strongly temperature dependent. Higher temperatures accelerate kinetics and shift the equilibrium towards products; NH_3 conversion to

H_2 is more complete, sustaining electrochemical performance. NH_3 utilization ranges from 9.6% at 680K to 100% at 816K.

3.4) Future Implementation

The architectural decisions made during model development were guided by the requirements of system-level analysis. The developed model enables simulation of PCFCs under lower computational intensity while capturing spatially evolving nature of fuel cell operation. This approach is highly relevant, especially when simulating complex system setups as it provides more representative results than 0-D models while avoiding increased convergence times of 2-D and 3-D models.

Additionally, several steps have been taken to minimize model stiffness, including hyperbolic tangent smoothing and the application of physical bounds on key variables. A thermal fluid system before the introduction of the PCFC's may already be stiff, especially when containing multiple components and complex flow configurations. Introducing a stiff fuel cell model into the pre-existing system configuration adds an additional degree of complexity which may render the model unusable. Introducing these numerical approaches allows the model to yield meaningful results that can be used to assess whether the specified operating conditions correspond to realistic operation, instead of resulting in undefined solutions when the model diverges.

However, the model still has certain limitations which need to be addressed before implementing into system level analysis. Under reduced regularization factor eps, the system becomes unstable and often fails to converge. Under the lowest stable

regularization factor, the partial pressure dependent values such as the concentration overpotential still reach an upper boundary and cannot become the dominant loss mechanism. The electrochemistry still does not fully capture the mixed ionic electron conduction. While more complex models typically mechanistically capture MIEC through lattice defect conservation equations. Zhang et. al. developed an analytical expression for current leakage, derived as a function of gas composition gradients, electrolyte conductivities, and external current density, computing the impact current leakage on performance losses.

Additionally, the Fickian diffusion calculations for the species partial pressures may not fully capture the interactions between nitrogen, hydrogen, and ammonia in the anode. A more detailed transport model may implement Stefan–Maxwell type diffusion calculations to account for multicomponent effects, or use corresponding effective diffusion coefficients within a Fickian framework.

Defining an average cell current density and computing a corresponding cell voltage enables the simulation of spatially varying current density profiles under a uniform cell voltage assumption. However, this approach may enforce operating conditions that are not physically possible under real-world constraints, particularly under transport-limited operation. Introducing a charge conservation submodel would allow for the simulation of dynamically evolving voltage and current distributions throughout the cell, thus removing the dependence on a prescribed average current density. This approach more closely reflects the physical behavior of fuel cells, where current distribution emerges from local

electrochemical and transport processes, albeit at the cost of increased model complexity.

Overall, the developed model may be used to generate datasets for integration into Aspen HYSYS, or be adapted into Aspen Custom Modeler for more detailed mechanistic implementation. The solver structure can be transferred to ACM, as the Python-based formulation follows an equation-oriented architecture consistent with ACM's solving framework. ACM provides a flexible environment for implementing first-principles models and custom unit operations, which can subsequently be embedded into HYSYS. This enables coupling of detailed cell-level physics with system-level process simulation, leveraging HYSYS's extensive library of process components.

References

[1] “Climate change: global temperature | NOAA Climate.gov.” Accessed: Mar. 29, 2026. [Online]. Available: https://www.climate.gov/news-features/understanding-climate/climate-change-global-temperature?jr_id=l_4354547151

[2] “Images and Media: ClimateDashboard-global-surface-temperature-graph-20220624-1400px.jpg | NOAA Climate.gov.” Accessed: Apr. 24, 2026. [Online]. Available: https://www.climate.gov/media/12885

[3] “CO2 Emissions – Global Energy Review 2025 – Analysis,” IEA. Accessed: May 05, 2026. [Online]. Available: https://www.iea.org/reports/global-energy-review-2025/co2-emissions

[4] I. Staffell *et al.*, “The role of hydrogen and fuel cells in the global energy system”, doi: 10.1039/C8EE01157E.

[5] I. Sebbani, M. K. Ettouhami, and M. Boulakhbar, “Fuel cells: A technical, environmental, and economic outlook,” *Clean. Energy Syst.*, vol. 10, p. 100168, Jun. 2025, doi: 10.1016/j.cles.2024.100168.

[6] K. G. Nandi Rakesh, “Fuel Cell Market Size & Share, YoY Growth Scope | 2035,” Claight Corporation (Expert Market Research). Accessed: Apr. 12, 2026. [Online]. Available: https://www.expertmarketresearch.com/reports/fuel-cell-market

[7] L. Fan, Z. Tu, and S. H. Chan, “Recent development of hydrogen and fuel cell technologies: A review,” *Energy Rep.*, vol. 7, pp. 8421–8446, Nov. 2021, doi: 10.1016/j.egyr.2021.08.003.

[8] N. Q. Minh, “Solid oxide fuel cell technology—features and applications,” *Solid State Ion.*, vol. 174, no. 1, pp. 271–277, Oct. 2004, doi: 10.1016/j.ssi.2004.07.042.

[9] H. Sumi *et al.*, “Oxygen reduction kinetics of high performance BaCo0.4Fe0.4M0.1Y0.1O3-δ (M = Mg, Zr) positrode for protonic ceramic fuel cells,” *Commun. Chem.*, vol. 8, no. 1, p. 71, Mar. 2025, doi: 10.1038/s42004-025-01468-4.

[10] F. Liu *et al.*, “Lowering the operating temperature of protonic ceramic electrochemical cells to <450 °C,” *Nat. Energy*, vol. 8, no. 10, pp. 1145–1157, Oct. 2023, doi: 10.1038/s41560-023-01350-4.

[11] A. K. Azad *et al.*, “Improved mechanical strength, proton conductivity and power density in an ‘all-protonic’ ceramic fuel cell at intermediate temperature,” *Sci. Rep.*, vol. 11, no. 1, p. 19382, Sep. 2021, doi: 10.1038/s41598-021-98987-6.

[12] T. T. Le *et al.*, “Fueling the future: A comprehensive review of hydrogen energy systems and their challenges,” *Int. J. Hydrog. Energy*, vol. 54, pp. 791–816, Feb. 2024, doi: 10.1016/j.ijhydene.2023.08.044.

[13] A. Züttel, “Hydrogen storage methods,” *Naturwissenschaften*, vol. 91, no. 4, pp. 157–172, Mar. 2004, doi: 10.1007/s00114-004-0516-x.

[14] M. R. Usman, “Hydrogen storage methods: Review and current status,” *Renew. Sustain. Energy Rev.*, vol. 167, p. 112743, Oct. 2022, doi: 10.1016/j.rser.2022.112743.

[15] M. Zacarias and J. Nakano, “Exploring the Hydrogen Midstream: Distribution and Delivery”, Accessed: Apr. 17, 2026. [Online]. Available: https://www.csis.org/analysis/exploring-hydrogen-midstream-distribution-and-delivery?utm_source=chatgpt.com

[16] L. Zhu *et al.*, “Ammonia-fed reversible protonic ceramic fuel cells with Ru-based catalyst,” *Commun. Chem.*, vol. 4, no. 1, p. 121, Aug. 2021, doi: 10.1038/s42004-021-00559-2.
[17] C. Duan *et al.*, “Highly durable, coking and sulfur tolerant, fuel-flexible protonic ceramic fuel cells,” *Nature*, vol. 557, no. 7704, pp. 217–222, May 2018, doi: 10.1038/s41586-018-0082-6.
[18] J. Norman, A. Yousuf, C. Duan, H. Ding, H. Shabgard, and P. Kazempoor, “Dual-function protonic ceramic fuel cell for efficient natural gas conversion to power and chemicals,” *Chem. Eng. J.*, vol. 507, p. 160527, Mar. 2025, doi: 10.1016/j.cej.2025.160527.
[19] “Ammonia pipelines: existing networks, future deployments, and safety considerations,” Ammonia Energy Association. Accessed: Apr. 17, 2026. [Online]. Available: https://ammoniaenergy.org/articles/ammonia-pipelines-existing-networks-future-deployments-and-safety-considerations/
[20] “Ammonia’s Role in a Net-Zero Hydrogen Economy,” Kleinman Center for Energy Policy. Accessed: Apr. 17, 2026. [Online]. Available: https://kleinmanenergy.upenn.edu/research/publications/ammonias-role-in-a-net-zero-hydrogen-economy/
[21] A. C. Chien, W. Y. Chen, and M. S. Zheng, “Direct Conversion of Ammonia to Electricity on a PCFC and an SOFC,” *J. Electrochem. Soc.*, vol. 170, no. 4, p. 044505, Apr. 2023, doi: 10.1149/1945-7111/accbef.
[22] H. Zhu, C. Karakaya, and R. J. Kee, “Modeling ammonia-fueled co-flow dual-channel protonic-ceramic fuel cells,” *Int. J. Green Energy*, vol. 19, no. 14, pp. 1568–1582, Nov. 2022, doi: 10.1080/15435075.2021.2018321.
[23] Z. Li *et al.*, “Direct ammonia protonic ceramic fuel cell: A modelling study based on elementary reaction kinetics,” *J. Power Sources*, vol. 556, p. 232505, Feb. 2023, doi: 10.1016/j.jpowsour.2022.232505.
[24] H. Zhu, P. Zhao, Z. Shi, W. Xue, and J. Wang, “4E performance analysis and multi-objective optimization of a power-heat-freshwater trigeneration system based on ammonia-fed protonic ceramic fuel cell, micro gas turbine, and air gap membrane distillation,” *Energy Convers. Manag.*, vol. 336, p. 119867, Jul. 2025, doi: 10.1016/j.enconman.2025.119867.
[25] C. Wang, J. Fan, Y. Xing, and J. Guan, “Thermodynamics and electrochemical performance of co- and counter-flow planar solid oxide fuel cells under an adiabatic operation environment,” *Int. J. Hydrog. Energy*, vol. 50, pp. 181–199, Jan. 2024, doi: 10.1016/j.ijhydene.2023.08.094.
[26] “Optimization and root finding (scipy.optimize) — SciPy v0.15.1 Reference Guide.” Accessed: Apr. 16, 2026. [Online]. Available: https://docs.scipy.org/doc/scipy-0.15.1/reference/optimize.html
[27] S. Catsis, C. L. Hall, and M. R. Jeffrey, “The hidden sensitivity of non-smooth dynamics,” *Phys. Nonlinear Phenom.*, vol. 463, p. 134165, Jul. 2024, doi: 10.1016/j.physd.2024.134165.

[28] K. J. Albrecht, C. Duan, R. O'Hayre, and R. J. Braun, "Modeling Intermediate Temperature Protonic Ceramic Fuel Cells," *ECS Trans.*, vol. 68, no. 1, p. 3165, Jun. 2015, doi: 10.1149/06801.3165ecst.
[29] P. Aguiar, C. S. Adjiman, and N. P. Brandon, "Anode-supported intermediate temperature direct internal reforming solid oxide fuel cell. I: model-based steady-state performance," *J. Power Sources*, vol. 138, no. 1, pp. 120–136, Nov. 2004, doi: 10.1016/j.jpowsour.2004.06.040.
[30] A. T. Schmidt, "DYNAMIC MODELING OF SOLID OXIDE FUEL CELL SYSTEMS FOR COMMERCIAL BUILDING APPLICATIONS".
[31] P. Kazempoor and R. J. Braun, "Model validation and performance analysis of regenerative solid oxide cells for energy storage applications: Reversible operation," *Int. J. Hydrog. Energy*, vol. 39, no. 11, pp. 5955–5971, Apr. 2014, doi: 10.1016/j.ijhydene.2014.01.186.
[32] M. A. Qadeer *et al.*, "A review on fundamentals for designing hydrogen evolution electrocatalyst," *J. Power Sources*, vol. 613, p. 234856, Sep. 2024, doi: 10.1016/j.jpowsour.2024.234856.
[33] H. Zhu, Y. Shin, S. Ricote, and R. J. Kee, "Thermodynamics, Transport, and Kinetics in BaZr0.8Y0.2O3−δ Electrolytes and their Impact on Hydrogen Separation and Compression," *J. Electrochem. Soc.*, vol. 170, no. 6, p. 064501, Jun. 2023, doi: 10.1149/1945-7111/acd8f6.
[34] Y. Sahli, "Thermodynamic Modeling and Analysis of Proton Ceramic Fuel Cells: Power Optimization," *Arab. J. Sci. Eng.*, vol. 47, no. 5, pp. 6355–6363, Nov. 2021, doi: 10.1007/s13369-021-06262-7.
[35] Y. Okuyama *et al.*, "Analyzing elementary electrode reactions for protonic ceramic fuel cells by proton/deuteron isotope effect," *J. Power Sources*, vol. 586, p. 233647, Dec. 2023, doi: 10.1016/j.jpowsour.2023.233647.
[36] S. H. Chan, K. A. Khor, and Z. T. Xia, "A complete polarization model of a solid oxide fuel cell and its sensitivity to the change of cell component thickness," *J. Power Sources*, vol. 93, no. 1, pp. 130–140, Feb. 2001, doi: 10.1016/S0378-7753(00)00556-5.
[37] R. Suwanwarangkul, E. Croiset, M. W. Fowler, P. L. Douglas, E. Entchev, and M. A. Douglas, "Performance comparison of Fick's, dusty-gas and Stefan–Maxwell models to predict the concentration overpotential of a SOFC anode," *J. Power Sources*, vol. 122, no. 1, pp. 9–18, Jul. 2003, doi: 10.1016/S0378-7753(02)00724-3.
[38] S. Campanari and P. Iora, "Comparison of Finite Volume SOFC Models for the Simulation of a Planar Cell Geometry," *Fuel Cells*, vol. 5, no. 1, pp. 34–51, 2005, doi: 10.1002/fuce.200400057.
[39] A. Gancarczyk *et al.*, "Heat and Momentum Transfer Analogies in Laminar Flow," *J. Heat Transf.*, vol. 141, no. 024502, Nov. 2018, doi: 10.1115/1.4041799.
[40] O. Elmutasim, D. S. Dhawale, M. Pinczes, S. Giddey, G. Paul, and S. Bhattacharya, "Mechanistic Investigation of Ammonia Utilization Pathways on a Locally Oxygen Enriched Ni–YSZ Anode for Direct Ammonia-Fed Solid Oxide Fuel Cells: An Ab Initio Study," *ACS Sustain. Chem. Eng.*, vol. 13, no. 42, pp. 18242–18254, Oct. 2025, doi: 10.1021/acssuschemeng.5c07973.

[41] Y. Kalinci and I. Dincer, “Analysis and performance assessment of NH3 and H2 fed SOFC with proton-conducting electrolyte,” *Int. J. Hydrog. Energy*, vol. 43, no. 11, pp. 5795–5807, Mar. 2018, doi: 10.1016/j.ijhydene.2017.07.234.
[42] Y. Aoki, T. Yamaguchi, S. Kobayashi, D. Kowalski, C. Zhu, and H. Habazaki, “High-Efficiency Direct Ammonia Fuel Cells Based on BaZr0.1Ce0.7Y0.2O3− δ/Pd Oxide-Metal Junctions,” *Glob. Chall.*, vol. 2, no. 1, p. 1700088, Dec. 2017, doi: 10.1002/gch2.201700088.
[43] K. Okura, K. Miyazaki, H. Muroyama, T. Matsui, and K. Eguchi, “Ammonia decomposition over Ni catalysts supported on perovskite-type oxides for the on-site generation of hydrogen”, doi: 10.1039/C8RA06100A.
[44] T. E. Bell and L. Torrente-Murciano, “H2 Production via Ammonia Decomposition Using Non-Noble Metal Catalysts: A Review,” *Top. Catal.*, vol. 59, no. 15, pp. 1438–1457, Jul. 2016, doi: 10.1007/s11244-016-0653-4.
[45] R. B. Barat, “Simple Rate Expression for Catalyzed Ammonia Decomposition for Fuel Cells,” *Molecules*, vol. 28, no. 16, p. 6006, Aug. 2023, doi: 10.3390/molecules28166006.
[46] M. W. Chase, “NIST-JANAF Themochemical Tables, Fourth Edition,” *J. Phys. Chem. Ref. Data, Monograph* 9, pp. 1–1951, 1998.
[47] “Chapter 2: Fuel Cell Thermodynamics,” in *Fuel Cell Fundamentals*, John Wiley & Sons, Ltd, 2016, pp. 25–76. doi: 10.1002/9781119191766.ch2.
[48] Z. Huang *et al.*, “Large-area anode-supported protonic ceramic fuel cells combining with multilayer-tape casting and hot-pressing lamination technology,” *J. Eur. Ceram. Soc.*, vol. 43, no. 2, pp. 428–437, Feb. 2023, doi: 10.1016/j.jeurceramsoc.2022.09.057.
[49] Z. Li *et al.*, “Effects of cathode thickness and microstructural properties on the performance of protonic ceramic fuel cell (PCFC): A 3D modelling study,” *Int. J. Hydrog. Energy*, vol. 47, no. 6, pp. 4047–4061, Jan. 2022, doi: 10.1016/j.ijhydene.2021.11.022.
[50] F. He *et al.*, “A New Pd Doped Proton Conducting Perovskite Oxide with Multiple Functionalities for Efficient and Stable Power Generation from Ammonia at Reduced Temperatures,” *Adv. Energy Mater.*, vol. 11, no. 19, p. 2003916, 2021, doi: 10.1002/aenm.202003916.
[51] K. Khan *et al.*, “Design of efficient and durable symmetrical protonic ceramic fuel cells at intermediate temperatures via B-site doping of Ni in BaCe0.56Zr0.2Ni0.04Y0.2O3–δ,” *Ceram. Int.*, vol. 49, no. 11, Part A, pp. 16826–16835, Jun. 2023, doi: 10.1016/j.ceramint.2023.02.043.